Published in final edited form as:

Nat Microbiol. 2024 April ; 9(4): 949–963. doi:10.1038/s41564-024-01641-w.

Tollip inhibits lipid accumulation and the integrated stress response in alveolar macrophages to control mycobacterium tuberculosis infection

Sambasivan Venkatasubramanian[1], **Courtney R. Plumlee**[2], **Kimberly A. Dill-McFarland**[1], **Sara B. Cohen**[2], **Benjamin H. Gern**[2,3], **Divya A Rane**[1], **Mackenzie K. Meyer**[1], **Aparajita Saha**[1], **Sarah A. Hinderstein**[1], **Gemma L. Pearson**[4], **Anne C. Lietzke**[4], **Amanda Pacheco**[4], **Yu-Hua Chow**[1], **Chi F. Hung**[1], **Scott A. Soleimanpour**[4,5], **Matthew Altman**[1], **Kevin B. Urdahl**[2,6], **Javeed A. Shah**[1,7,*]

[1]Department of Medicine, University of Washington, Seattle, WA.

[2]Seattle Children's Research Institute, Seattle, WA.

[3]Department of Pediatrics, University of Washington, Seattle, WA.

[4]Department of Internal Medicine, University of Michigan, Ann Arbor, MI.

[5]VA Ann Arbor Healthcare System, Ann Arbor, MI.

[6]Departments of Pediatrics and Immunology, University of Washington, Seattle, WA.

[7]VA Puget Sound Healthcare System, Seattle, WA.

Abstract

A polymorphism causing deficiencies in Toll-Interacting Protein (TOLLIP), an inhibitory adaptor protein affecting endosomal trafficking, is associated with increased tuberculosis (TB) risk. It is, however, unclear how TOLLIP affects TB pathogenesis. Here we show that TB severity is increased in *Tollip*$^{-/-}$ mice, characterized by macrophage- and T cell-driven inflammation, foam cell formation and lipid accumulation. *Tollip*$^{-/-}$ alveolar macrophages (AM) specifically accumulated lipid and underwent necrosis. Transcriptional and protein analyses of *Mycobacterium tuberculosis* (Mtb)-infected, *Tollip*$^{-/-}$ AM revealed increased EIF2 signaling, and downstream upregulation of the integrated stress response (ISR). These phenotypes were linked, as incubation of the Mtb lipid mycolic acid with Mtb-infected *Tollip*$^{-/-}$ AM activated the ISR and increased Mtb replication. Correspondingly, the ISR inhibitor, ISRIB, reduced Mtb numbers in AM and improved Mtb control, overcoming the inflammatory phenotype. In conclusion, targeting the ISR offers a

* jashah@uw.edu .

Author Contributions: Each author provided the following contribution to this study: Conceptualization: SV, KU, SS, JS; methodology: SV, SS, KU, MA, SD, JS; resources: JS, SS software: KDM, MA; validation: SV, JS, AS; formal analysis: MA, KDM, BG; investigation: SV, SH, CP, GP, AL, AP, RP, JS, BG, DAR, MKM, AS, YC, CFH; writing – original draft: SV, JS; writing – review and editing: KU, SS, MA, DAR, CP, JS; supervision: JS, KU, MA, SS, BG, CFH; project administration: SV, JS; funding acquisition: JS, KU, SS, MA, BG.

Competing Interest Statement: The authors declare no competing interests.

Code Availability

All custom scripts have been made available at https://github.com/altman-lab/Shah_mouse_collab. Additional modified scripts can be accessed upon request.

promising target for host-directed anti-TB therapy towards improved Mtb control and reduced immunopathology.

Introduction

A common, functional promoter variant in Toll-Interacting Protein (TOLLIP) is associated with *TOLLIP* deficiency and increased risk for *Mycobacterium tuberculosis* (Mtb) disease [1, 2, 3]. TOLLIP is a ubiquitin-binding protein, expressed in all tissues, that organizes the transport and delivery of endosomal cargo[4, 5]. Its cargo include intracellular lipids[6], insoluble protein aggregates[7, 8], cell surface and endosomal signaling receptors[9], and mitochondria[10, 11], but its complex and varied role in endosomal transport remains incompletely defined. Via this activity, TOLLIP diminishes TLR2, TLR4, and IL1-R signaling, stabilizes Type I interferon secretion via the endosomal immune receptor STING, and significantly reduces immune pathology during prolonged LPS stimulation[9, 12, 13, 14, 15]. TOLLIP influences pathogenesis of several chronic conditions, including neurodegenerative disease[7], pulmonary fibrosis[16], stroke[17], and myocardial infarction[18]. Thus, TOLLIP regulates a plethora of diverse cellular functions and pathological conditions, but how it influences Mtb pathogenesis is unknown.

Macrophages are good candidate mediators for tuberculosis (TB) susceptibility in TOLLIP-deficient individuals. Macrophages are the primary intracellular niche for Mtb *in vivo*, and the relative activation state of the macrophage determines whether this niche is permissive or restrictive to Mtb replication. Alveolar macrophages (AM) are the first cells infected by Mtb and are a preferred replicative niche. Intrinsic macrophage factors interpret inflammatory signals from multiple cytokines and cell populations to harness immune signals to restrict Mtb growth, or undergo necrosis, release Mtb into the extracellular space, and permit ongoing replication [19, 20, 21, 22]. TOLLIP's diverse functions significantly overlap with critical host defense pathways responsible for Mtb control. TLR2, TLR4, IL-1R, and STING participate in Mtb recognition by innate immune cells and contribute to Mtb host defense[23, 24, 25]. Complex ER endosomal sorting restricts intracellular Mtb growth[26], and oxidative damage from senescent mitochondria induces Mtb spread in macrophages[20, 27]. Accumulation of lipids and insoluble protein aggregates within macrophages leads to foamy macrophage formation and Mtb persistence *in vivo*, which may influence macrophage sensitivity to inflammation[21, 28, 29]. Therefore, understanding how TOLLIP restricts Mtb growth or permits necrosis within macrophages may provide insight into essential Mtb host response pathways, especially during chronic infection. To better understand how TOLLIP influences Mtb-macrophage interactions *in vivo*, we conducted a series of experiments in genetically modified mice to identify the lung-resident macrophage subsets most dependent on TOLLIP for Mtb host defense and the specific cellular mechanisms responsible for this phenotype.

Results

TOLLIP is required to control Mtb infection

Human TOLLIP-deficient peripheral blood macrophages developed hyperinflammatory cytokine responses after TLR stimulation or live Mtb infection[1, 3]. We hypothesized that murine TOLLIP deficiency might be linked to similarly dysregulated cytokine responses. *Tollip*$^{-/-}$ peritoneal macrophages (PEM) secreted more TNF but less IL-10 after LPS (TLR4 ligand), PAM3 (TLR2/1 ligand), or Mtb whole cell lysate stimulation (Extended Data 1A–B), and more TNF and IL-1β but less IL-10, after Mtb infection (Extended Data 1C–E; H37Rv strain, MOI 2.5). *Tollip*$^{-/-}$ mice demonstrated similar proportions of total splenic immune cells, T cells, NK cells, and macrophages as littermate controls (B6; Extended Data 1F–G). We noted a modest but statistically significant increase in the total proportion of alveolar macrophages (AM) in healthy *Tollip*$^{-/-}$ mice (Extended Data 1H). These findings are consistent with our prior studies and suggest that *Tollip* regulates macrophage function similarly in humans and mice, resolving an ongoing debate[30].

Human TOLLIP deficiency is associated with increased risk for TB disease, so we hypothesized that *Tollip*$^{-/-}$ mice also developed worsened Mtb disease. We infected *Tollip*$^{-/-}$ mice with ~50 colony forming units (CFU) of Mtb H37Rv via aerosol and monitored weight, bacterial burden, and survival over time (Figure 1A). *Tollip*$^{-/-}$ mice developed increased bacillary burden in their lungs and spleen 56 days post-infection and onward (Figure 1B–C). *Tollip*$^{-/-}$ mice exhibited greater weight loss and met criteria for euthanasia before B6 littermates (Figure 1D–E). Histopathologic analysis of lung sections revealed distinct patterns in *Tollip*$^{-/-}$ mice 56 days after infection, displaying increased numbers of inflammatory infiltrating cells with finely fibrillary cytoplasmic appearance, potentially consistent with excess lipid-laden “foamy” macrophages. *Tollip*$^{-/-}$ mice demonstrated increased intracellular and extracellular lipid deposition using fluorescent lipid stains (Figure 1F–H). Taken together, *Tollip*$^{-/-}$ mice developed worsened Mtb disease, with large numbers of foamy macrophages and lipid deposition.

Lung-resident macrophage subset populations demonstrate distinct characteristics that influence Mtb responses [31]. Therefore, we tracked Mtb at a cellular level by infecting mice with Mtb expressing an mCherry fluorescent reporter (Mtb-mCherry; gating in Extended Data 2A–F). Similar proportions of AM (CD11c+SiglecF+), monocyte-derived macrophages (MDM; SiglecF−CD11b+CD11c+MHCII+), interstitial macrophages (IM; SiglecF−CD11b+CD11c−MHCII+), neutrophils (PMN; SiglecF−CD11b+Ly6G+), and dendritic cells (DC; SiglecF−CD11b−CD11c+MHCII+) were infected with Mtb-mCherry 28 days post infection (Figure 1I), but after 56 days, we noted significantly greater proportion of Mtb-infected *Tollip*$^{-/-}$ AM (Figure 1J, Extended Data 2G). *Tollip*$^{-/-}$ and B6 mice exhibited similar proportions of AM, MDM, IM, PMN, and DC 28 and 56 days after infection (Extended Data 2H–I)[32, 33].

T cells are a critical component of Mtb host defense, and TOLLIP variants are associated with diminished mycobacteria-specific CD4+ T cell responses in infants[2]. We characterized Mtb-specific CD4+ T cell responses with MHC-II tetramers recognizing the immunodominant ESAT-6 epitope[34]. In B6 mice, day 28–34 after Mtb infection

generally represents the peak of the CD4+ T cell response, while day 56 begins a plateau, which persists for at least 300 days after infection[34]. In *Tollip*$^{-/-}$ mice, the proportion of ESAT-6+CD44+CD4+ T cells were diminished 28 and 56 days after infection (Figure 1K–L), while the proportion of maladaptive, terminally-differentiated ESAT-6+KLRG-1+PD1-CD44+CD4+ T cells increased over time (Figure 1M–N) [34]. Taken together, Mtb-infected, *Tollip*$^{-/-}$ mice recapitulate key clinical and immune findings observed in human genetic studies [1, 2] and are a model of excess macrophage and T cell inflammation during chronic Mtb infection.

Tollip$^{-/-}$ *alveolar macrophages selectively undergo necrosis*

We next evaluated the contribution of abnormal T cell and macrophage responses in *Tollip*$^{-/-}$ mice to Mtb outcomes. TOLLIP mRNA and protein expression is ubiquitous in both hematopoietic and non-hematopoietic cells[4, 35]. To assess the relative contribution of hematopoietic cells to Mtb immunity, we generated bone-marrow chimeric mice and infected them with aerosolized Mtb. Bacterial burdens were determined 60 days after infection (Figure 2A). *Tollip*$^{-/-}$ bone marrow → *Tollip*$^{-/-}$ mice exhibited higher lung bacterial burdens that B6 → B6 controls. *Tollip*$^{-/-}$ → B6 chimeras developed elevated bacterial burden, while bacillary load in B6 → *Tollip*$^{-/-}$ was not significantly different than B6 → B6 controls (Figure 2B). Therefore, TOLLIP influences Mtb protection via expression in radiosensitive hematopoietic cells.

We measured the contribution of *Tollip*$^{-/-}$ T cells to worsened Mtb disease. We created T-cell specific chimeric mice via sublethal irradiation of *B6.129P2-Tcrb*^{tm1Mom} *Tcrd*^{tm1Mom}*/J* (β-/δ-TCR.Tg) mice, which lack effective mature T cells, and transplanted bone marrow from B6 or *Tollip*$^{-/-}$ mice to create T cell-specific chimeras. These chimeras contain ~98% of donor T cells[36]. *Tollip*$^{-/-}$ T cell chimeric mice demonstrated no difference in Mtb CFU in the lung 56 days after infection (Figure 2C), indicating that Mtb susceptibility in *Tollip*$^{-/-}$ mice was mediated by factors extrinsic to T cells.

We also measured Mtb pathogenesis in lung macrophages in the absence of T or B cell help. We compared Mtb burden and intracellular Mtb-mCherry carriage in lung-resident macrophages between *Tollip*$^{+/+}$, *Tollip*$^{-/-}$, *Rag1*$^{-/-}$, and *Rag1*$^{-/-}$*Tollip*$^{-/-}$ mice 28 and 44 days after aerosol infection. After 28 days, *Rag1*$^{-/-}$*Tollip*$^{-/-}$ mice demonstrated increased Mtb CFU in their lungs (2.2x higher CFU) compared to *Rag1*$^{-/-}$ mice (Figure 2D), but by 44 days, both *Rag1*$^{-/-}$ and *Rag1*$^{-/-}$*Tollip*$^{-/-}$ mice became moribund. The frequency of Mtb-infected AM, but not MDM or PMN, were significantly increased in *Rag1*$^{-/-}$*Tollip*$^{-/-}$ mice both 28 and 44 days after Mtb-mCherry infection (Figure 2E–F, representative images, Figure S2J). The selective difference in Mtb carriage in AM between *Rag1*$^{-/-}$ mice and *Rag1*$^{-/-}$*Tollip*$^{-/-}$ may indicate altered macrophage host defense. Overall, *Tollip*$^{-/-}$ myeloid cells and T cells are hyperinflammatory and both cell types contribute to worsened Mtb disease. Excess inflammation from T cells and macrophages worsens Mtb severity by inducing necrosis in Mtb-infected cells [20, 22]. Mtb-infected macrophages integrate signals across multiple cell types, leading to either Mtb control or cellular necrosis to permit Mtb escape. *Tollip* influences endocytosis to macrophage cell death, so we investigated whether immune pathology in *Tollip*$^{-/-}$ mice was due to excess inflammation increased sensitivity to

inflammatory signals[5, 37]. We generated mixed bone marrow chimeric mice to test whether *Tollip*$^{-/-}$ macrophages in a cell-autonomous fashion, independently of the magnitude of T cell or macrophage-induced cytokines. B6.SJL-*Ptprca Pepcb/BoyJ* (CD45.1) mice were lethally irradiated and bone marrow was reconstituted with a 1:1 mix of *Tollip*$^{-/-}$ (CD45.2+) and F1 B6 (CD45.1+CD45.2+) bone marrow, followed by 10 weeks of rest (Figure 2G). After confirming equal proportions of immune cells from each lineage (Figure 2H), we infected chimeras with Mtb-mCherry and compared the proportion of Mtb-infected myeloid cell subsets by genotype over time (gating strategy depicted in Extended Data 3A). AM were the primary cell infected 14 days post-infection, with increasing proportions of PMN and MDM becoming infected over time, consistent with prior findings (Figure 2I)[33]. We also evaluated the sensitivity of dendritic cells (SiglecF−CD11b−MHCII+CD11c+ cells) to inflammatory signaling. This population was rare (<1% frequency), had low proportional Mtb infection (< 0.3% Mtb+), and we detected no differences in Mtb carriage based on the presence of *Tollip*, so this population was excluded (data not shown). 28 days after infection, proportionally more *Tollip*$^{-/-}$ AM were Mtb infected and intracellular Mtb MFI was increased (Figure 2J–K, representative images, Extended Data 3A). After 56 days of infection, fewer *Tollip*$^{-/-}$ AM were proportionally infected with Mtb, measured both by percentage of mCherry+ cells and total CFU / cell from sorted AM and MDM (Figure 2L–M, representative images Figure 2N). These data demonstrate diminished Mtb carriage in *Tollip*$^{-/-}$ AM due to intrinsic factors.

In prior studies, diminished proportional Mtb infection in macrophages, in the setting of worsened disease, was associated with increased cellular necrosis[19, 38]. In mixed bone marrow chimeras, *Tollip*$^{-/-}$ AM had reduced apoptosis and unchanged necrosis 28 days after infection (Figure 3A) and selectively increased necrosis 56 days after infection (Figure 3B). Overall, *Tollip*$^{-/-}$ AM selectively developed diminished apoptosis and increased necrosis after prolonged Mtb infection.

AM are comprised of two ontologically and functionally distinct subpopulations, tissue-resident AM (TR-AM) and monocyte-derived AM (Mo-AM)[39]. TR-AM are derived from fetal liver and replenish within lung tissue, while Mo-AM develop from bone marrow and traffic to lung in response to injury[39, 40]. As Mo-AM dominate AM reconstitution after irradiation, we defined whether TOLLIP's effects were generalizable to all AM via adoptive transfer. We intratracheally instilled 10^5 B6 (CD45.2+) or *Tollip*$^{-/-}$ (CD45.2+) AM into CD45.1+ recipient mice 72hr after liposomal clodronate treatment to deplete native AM, allowed 14 days for AM reconstitution, then infected with Mtb for 56 days (Figure 3C, experimental outline, representative image in Extended Data 3E). Transferred *Tollip*$^{-/-}$ AM developed increased cell necrosis and diminished apoptosis compared to native CD45.1+ AM after 56 days of Mtb infection (Figure 3D), while B6 AM transferred into CD45.1 mice demonstrated no significant differences in cell death (Figure 3E). In summary, *Tollip*$^{-/-}$ AM are selectively and autonomously susceptible to Mtb-induced necrosis.

Tollip$^{-/-}$ *AM develop increased EIF2 signaling*

Our observation that TOLLIP induced a cell-autonomous phenotype in AMs was somewhat surprising. Inflammation induced cell stress and death, particularly via TNF or IFNγ,

requires cellular cooperation via cytokine - receptor interaction, a characteristic of cell-extrinsic stimuli. The genetic factors that contribute to excess cellular necrosis in Mtb-infected macrophages are incompletely understood[21, 27], and those factors that selectively influence AM function are not known. Therefore, we investigated the molecular pathways that were responsible for selective cell death in *Tollip*$^{-/-}$ AM. Studying these pathways responsible for macrophage sensitivity may provide a mechanism for overcoming host inflammation, even from multiple sources. We compared the global transcriptional networks of sorted, Mtb-infected and bystander B6 and *Tollip*$^{-/-}$ AM from mixed bone marrow chimeric mice 28 days after Mtb infection to ensure robust mCherry fluorescence (sorting strategy is shown in Extended Data 4). We identified 194 differentially expressed genes (DEG) between B6 and *Tollip*$^{-/-}$ Mtb-infected AM (FDR < 0.05; gene names in Source Data 1) and 157 DEGs between B6 and *Tollip*$^{-/-}$ Mtb-uninfected "bystander" AM (Figure 4A; Dataset S1). We performed Ingenuity Causal Network Analysis comparing DEGs (FDR < 0.05) from Mtb-infected B6 and *Tollip*$^{-/-}$ AM[41]. The top node with a directional effect "Increased EIF2 Signaling" (Figure 4B). We also performed Gene Set Enrichment Analysis using Reactome gene sets, where two of the top six hits were "Cellular response to starvation" ($q = 1.06\times10^{-5}$) and "Response of EIF2AK4 (GCN2) to amino acid deficiency" ($q = 9.07\times10^{-5}$; Figure 4C)[42]. As EIF2AK4 is a kinase that activates EIF2 signaling, both approaches indicate that EIF2 signaling may be activated in *Tollip*$^{-/-}$ AM during Mtb infection. Specific DEGs contained in gene sets of interest are called in a heatmap (Figure 4D).

EIF2 activation occurs after phosphorylation at Ser51 and triggers the integrated stress response (ISR), a set of cellular adaptations to harsh environmental or cellular conditions[43]. Using mixed bone marrow chimeras and validated antibodies, we confirmed that pEIF2 protein was selectively and autonomously increased in *Tollip*$^{-/-}$ AM 28 and 56 days after infection (Figure 4E–F) and in TR-AM adoptively transferred into CD45.1+ mice (Figure 4G)[44]. In total lung tissue, we found broadly increased pEIF2 but not total EIF2A protein in *Tollip*$^{-/-}$ mice 56 days after aerosol Mtb infection (Figure 4H–J). Overall, *Tollip*$^{-/-}$ AM autonomously developed increased pEIF2, *Tollip*$^{-/-}$ mice exhibited global pEIF2 excess in their lungs, and excess pEIF2 correlated with clinical worsening of Mtb infection.

Mtb mycolates induce Mtb replication in Tollip$^{-/-}$ *macrophages*

We next investigated how *Tollip*$^{-/-}$ AM develop selectively increased ISR activity. *Tollip*$^{-/-}$ mice developed foam cells and lipid deposits in their lungs, and foam cells permit Mtb persistence and replication in macrophages[21, 29]. Foam cell formation requires cellular inflammation as well as aberrant lipid homeostasis[45]. In mixed bone marrow chimeric mice, *Tollip*$^{-/-}$ AM, but not MDM, autonomously accumulated excess lipid 28 days after Mtb infection, measured by median fluorescence of the LipidTox neutral lipid stain (Figure 5A–B). This observation led us to consider the relationship between TOLLIP, lipid accumulation, and ISR activation in Mtb-infected macrophages.

We evaluated the influence of TOLLIP on two known methods for inducing foam cell formation in Mtb-infected macrophages – stimulation of Mtb-infected cells with Type I interferons and administration of Mtb cell wall mycolic acids (MA)[46, 47]. *Ifnb1* gene

expression was diminished in Mtb-infected lung tissue from *Tollip*$^{-/-}$ mice 56 days after infection (Figure 5C)[14]. After TNF stimulation, *Ifnb1* was reduced *Tollip*$^{-/-}$ AM (Figure 5D), which is a measure of TNFR1 signaling and a mechanism for necrosis in Mtb-infected macrophages[46]. Overall, *Tollip*$^{-/-}$ AM demonstrated patent but not excessive TNFR signaling and diminished Type I interferon secretion after Mtb infection.

TOLLIP promotes lipid transport for autophagic degradation and recycles palmitic acid, a long-chain saturated fatty acid[6, 48]. MA is the commonest long-chain fatty acid in the Mtb cell wall[29]. Therefore, we hypothesized that aberrant lipid recycling in *Tollip*$^{-/-}$ macrophages promoted MA-induced lipid accumulation. We confirmed the capacity of *Tollip*$^{-/-}$ bone marrow-derived macrophages (BMDM) to perform bulk macroautophagy, a major lipid clearance pathway[49], by measuring LC3II and p62 protein after treatment with Bafilomycin A (BafA) to prevent autophagosome/lysosome fusion[50]. *Tollip* did not significantly affect levels of LC3II, the induction of LC3II, or the adaptor protein p62 by BafA treatment (Extended Data 5A–C). *Tollip*$^{-/-}$ PEM accumulated lipid droplets after treatment with MA for 72 hours (Figure 5E–G). *Tollip*$^{-/-}$ AM, but not MDM or PMN, accumulated lipids 5 days after intratracheal instillation of MA (Figure 5H).

We evaluated whether MA treatment selectively influenced *Tollip*$^{-/-}$ macrophage host defense. MA-treated *Tollip*$^{-/-}$ PEM and AM permitted increased replication, measured by luminescence, after infection with Mtb H37Rv expressing the *luxCDABE* luminescent reporter from *Vibrio harleyi* (Mtb-*lux*; MOI 1; Figure 5I–J)[2]. We replicated this result in human THP-1 macrophages lacking TOLLIP, which were previously developed in our lab (TOLLIP-KO; Figure 5K)[2]. MA treatment did not influence Mtb replication in BMDM (Figure 5LMA did not alter TNF secretion in any cell population (Extended Data 5D–F). In summary, MA treatment selectively leads to lipid accumulation and impaired Mtb host defense in *Tollip*$^{-/-}$ AM and PEM independently from proinflammatory cytokine responses. These effects were selective to these tissue-resident macrophage populations.

TOLLIP deficiency is associated with increased TB risk, and human macrophages lacking TOLLIP demonstrated increased Mtb replication *in vitro* after excess MA incubation. Therefore, we extended our observations to determine TOLLIP and ISR gene expression in human TB granulomas. TB granulomas develop strong inflammatory responses and lipid accumulation in the form of “caseum,” a lipid-rich center of necrosis, surrounded by foam cells and other inflammatory cells. Lipid accumulation may lead to suboptimal environmental conditions known the ISR. EIF2 is phosphorylated by one of four upstream kinases – *EIF2AK1* (HRI), *EIF2AK2* (PKR), *EIF2AK3* (PERK), and *EIF2AK4* (GCN2)[51]. We evaluated their gene expression, along with *TOLLIP*, in public data of human caseous granulomas compared with samples from healthy areas of the same lung [52]. *EIF2AK1*, *EIF2AK2*, *EIF2AK3, EIF2AK4, and TOLLIP* demonstrated increased expression in caseous granulomas (Figure 5M). In contrast, *TOLLIP* and EIF2 kinase expression was unchanged in the peripheral blood of individuals with active or latent TB (Extended Data 5G)[53]. EIF2 kinases and TOLLIP are selectively enriched human TB granulomas and may play a tissue-specific role during human TB disease.

ISR inhibition controls Mtb disease in vivo

After determining that lipid accumulation was associated with increased Mtb replication in *Tollip*$^{-/-}$ macrophages, we evaluated whether lipid excess may influence ISR activation by the expression of stress-related genes in MA-treated macrophages, as lipid excess induces endoplasmic reticulum stress[54, 55]. MA treatment of Mtb-infected, *Tollip*$^{-/-}$ PEM led to significant increases in *Ern1* (Extended Data 6A), *Eif2ak3,* which maintains immune function during lipid excess and activates the ISR (Extended Data 6B), and *Atf6* RNA transcript expression (Extended Data 6C), and induced pEIF2 expression via Western blot (Extended Data 6D). B6 PEM treated with the ISR activator raphin-1 (10μM) led to increased Mtb replication (Figure 6A), while treatment with the selective ISR inhibitor ISRIB (5nM) decreased Mtb replication in MA-treated, *Tollip*$^{-/-}$ PEM (Figure 6B), AM (Figure 6C) and THP-1 macrophages (Figure 6D)[56, 57]. Neither raphin-1 or ISRIB altered Mtb replication in broth culture (Figure S6E). ISRIB did not influence TNF secretion (Extended Data 6F–H). Overall, these data indicate that MA-induced Mtb replication in *Tollip*$^{-/-}$ macrophages is mediated through ISR activation.

Next, we tested the effectiveness of ISRIB on Mtb control *in vivo*. We infected mice with Mtb via aerosol, and after allowing 15 days for Mtb growth, treated daily with vehicle control, ISRIB (1mg/kg intraperitoneally), or raphin-1 (1mg/kg intraperitoneally). 56 days post infection, Mtb CFU were measured from lungs and spleen, and one lung lobe was preserved for pathology and spatial immunology analysis (Figure 6E). We visualized pEIF2 activation in Mtb-infected mice using multiplex confocal microscopy. Objects were first formed on CD68 signal to identify macrophages, then classified into AM (CD68+Siglec F+) and MDM (CD68+CD11b+; Extended Data 7A). We used histocytometry to identify antigen-bearing cells using an antibody generated against the purified protein derivative (PPD+), neutral lipid-bearing cells (LipidTox Red+), and pEIF2+ cells. (Extended Data 7B). Nearly all AM and MDM demonstrated pEIF2 activation, and ISRIB treatment diminished pEIF2 in AM and MDM, regardless of genotype (Extended Data 7C, representative images in Extended Data 7D). ISRIB treatment was associated with selective decrease in the frequency of PPD+ AM, but not spatial organization of macrophage populations (Figure 6F–G; 20μm spatial neighborhoods, Extended Data 7E). Lipid accumulation was observed predominantly in MDM but was detectable in AM. We correlated intracellular Mtb carriage in ISRIB-treated macrophages with overall Mtb burden. ISRIB restored Mtb control in the lungs and spleens of *Tollip*$^{-/-}$ mice, and reduced Mtb in resistant B6 control mice (Figure 6H–I). Raphin-1 increased Mtb burden in lungs and spleens of B6 mice (Figure 6J–K). ISRIB significantly reduced lung cellularity and overall inflammation score in *Tollip*$^{-/-}$ but not B6 mice (Figure 6L–N)[8]. In summary, ISRIB treatment selectively reduced the proportion of PPD+ AM after 56 days of infection, rescued the Mtb susceptibility phenotype and reduced inflammation in susceptible *Tollip*$^{-/-}$ mice, and significantly improved Mtb control in B6 mice.

Discussion

TOLLIP deficiency was associated with increased severity of Mtb disease. The worsened immunopathology in *Tollip*$^{-/-}$ mice was associated with excess macrophage cytokine

responses and T cell terminal differentiation, an abundance of lipid-laden foamy macrophages and failure to control Mtb replication during chronic infection. AM were cell-autonomous drivers of this phenotype, as AM lacking TOLLIP developed intracellular lipid accumulation, an EIF2-mediated stress response, and increased sensitivity to cellular necrosis in the setting of excess overall inflammation. EIF2 inhibition resulted in reduction of Mtb carriage in AM and improved overall Mtb control, providing a mechanistic link between TOLLIP deficiency and Mtb disease and identifying this pathway as a target for host-directed therapy.

A schematic of our proposed model is shown in Extended Data 8. *Tollip*$^{-/-}$ AM accumulate lipids intracellularly in the setting of excess inflammation during Mtb infection. Lipids and inflammation induce ISR activation and permit intracellular Mtb replication. During prolonged infection, excess ISR leads to necrosis and extracellular Mtb release in AM, while EIF2 inhibition via ISRIB restores host defense.

TOLLIP's effects on stress and host defense are stronger in AM than MDM, but we do not interpret this finding as a lack of effect in MDM. Instead, we predict that TOLLIP alters sensitivity to necrosis among all macrophages, but specific factors in AM, such as lipid storage, are cell-type specific effects that depend on the balance of uptake and breakdown. Preferential cell death in AM might be due to increased lipid uptake, diminished lipid catabolism, and macrophage subtypes demonstrate distinct homeostatic and metabolic characteristics[31]. Future studies will interrogate the impact of lipid accumulation and ISR inhibition on AM function directly,

Tollip$^{-/-}$ mice demonstrated increased EIF2 phosphorylation in AM, leading to immune pathology and Mtb progression. In prior studies, EIF2 was induced in Mtb-infected bone marrow-derived macrophages from *sst1.B6* mice that produce excess Type I interferon[46]. In our study, MA and TNF induced the ISR in Mtb-infected, *Tollip*$^{-/-}$ macrophages[47]. In models of hepatic steatosis and atherosclerosis, lipid accumulation in the ER induces EIF2 phosphorylation[58, 59]. Excess TNF induces programmed necrosis and Mtb spread by sphingosine-induced calcium flux and oxidative stress[27]. Notably, we found strong enrichment of lipid and sphingolipid metabolic transcriptional pathways in Mtb-infected *Tollip*$^{-/-}$ AM, and MA metabolizes into sphingosine in macrophages[60]. Future studies will interrogate the effect of excess lipid metabolites on AM function and ISR activation and their capacity to sensitize AM to necrosis via the ISR.

Intracellular Mtb burden within macrophages is an important measurement of Mtb host defense *in vivo*, but only describes a portion of the Mtb life cycle in the lung. Mtb replication occurs intracellularly, extracellularly, and within dead and dying macrophages[61]. Therefore, observations of intracellular Mtb within *Tollip*$^{-/-}$ macrophages must be made in the context of overall Mtb bacterial burden to consider extracellular Mtb release. 56 days after infection in mixed chimeras, *Tollip*$^{-/-}$ AM demonstrated diminished proportional carriage and increased Mtb burden. However, we observed reduced intracellular carriage in *Tollip*$^{-/-}$ AM and reduced Mtb burden during ISRIB treatment. Reduced carriage may be due to increased necrosis or improved host defense, which may include increased apoptosis, cell migration, or innate immune killing[19, 21, 62].

EIF2 activation and the downstream ISR may play an important role in the transition from asymptomatic Mtb infection to symptomatic TB disease. Studies from the preantibiotic era regularly describe “post-primary” tuberculosis as an acute, paucibacillary, caseating lipoid pneumonia obstructing bronchioles in a “tree-in-bud” pattern[63, 64]. Within the lipoid pneumonia, obstructed alveoli attract macrophages with a foamy appearance, leading to subsequent necrosis and granuloma formation. Pathologically, this obstructive lipid pneumonia precedes the transition from asymptomatic to symptomatic TB disease[65]. Our model mimics important aspects of this observation, whereby *Tollip*$^{-/-}$ AM accumulate lipid, which permits excess Mtb growth followed by necrosis via the EIF2 pathway. A combination of host and bacterial factors that obstruct clearance of lipid debris may contribute to Mtb progression by inducing EIF2.

We identified a critical role for TOLLIP within Mtb-infected AM that influences sensitivity to immune pathology. However, this study has limitations. Direct effects of soluble TNF and excess IFNγ on ISR activation contribute to TB susceptibility in hyperinflammatory *Tollip*$^{-/-}$ mice and overall pathology. However, this mechanism should not induce selective, cell-autonomous alteration in *Tollip*$^{-/-}$ AM, as TNFR signaling was not excessive in *Tollip*$^{-/-}$ AM. Reverse signaling (effects of TNF on the secreting cell) from transmembrane. Lipid accumulation and inflammation together induced the ISR in AM, but these are likely not the sole ISR activation signal. *Tollip*$^{-/-}$ cells demonstrate altered endocytosis, and abnormal endocytosis of variable cargo, like proteins and mitochondria, may also trigger the ISR. Future studies will define the specific contributions of inflammation, lipid, and other factors that impact ISR activation *in vivo*. *Tollip*$^{-/-}$ dendritic cells may induce excess T cell differentiation and worsen TB disease, and the contribution of terminal T cell differentiation to Mtb severity is well-established [34]. Therefore, we focused on cell populations that demonstrated impaired sensitivity to inflammation, with the hopes to overcome inflammatory signals from macrophages, T cells, and other immune cell types together. Future studies evaluating tissue-specific effects of critical ISR genes on Mtb pathogenesis will directly evaluate the impact of the ISR on these immune cell subpopulations. We assessed ISRIB activity during primary active TB infection. Determination of ISRIB’s clinical utility will require testing across multiple doses, during concurrent antimycobacterial therapy, and in more clinically relevant scenarios, such as preventing reactivation and progression of latent infection to acute disease.

ISR activation induces cellular necrosis in *Tollip*$^{-/-}$ AM during prolonged infection, providing a promising target for established disease. ISRIB enhanced Mtb control in *Tollip*$^{-/-}$ and B6 hosts by restoring AM host defense. Thus, ISRIB is a candidate host-directed therapeutic agent that should be explored further in future studies.

Methods

Ethics Statement

All experiments were performed in compliance with all relevant ethical regulations and was approved by the Institutional Animal Care and Use Committee from the University of Washington and the Seattle Children’s Research Institute.

Reagents

A complete list of reagents can be found in Supplementary Table 1.

Mice

All mice were housed and maintained in specific pathogen-free conditions at the University of Washington and Seattle Children's Research Institute. Mice used in the experiments were 6–12 weeks of age. B6.Cg-Tollip^{tm1Kbns}/Cnrm (*Tollip*$^{-/-}$) mice were obtained from the European Mutant Mouse Archive. Mice were backcrossed 11 times on C57BL/6J background and were confirmed to be >99% C57BL/6J genetically by screening 150 SNP ancestry informative markers (Jax, Inc). Genotyping was performed using DNA primers for neomycin (Forward sequence: AGG ATC TCC TGT CAT CTC ACC TTG CTC CTG; Reverse sequence AAG AAC TCG TCA AGA AGG CGA TAG AAG GCG) and the first exon of TOLLIP (Forward sequence: AGC TAC TGG GAG GCC ATA CA; Reverse sequence: CGT GTA CGG GAG ACC CAT TT). Protein expression was confirmed in both knockout and backcrossed alleles by qPCR and Western blot. All wild type control mice were age-matched littermates to ensure a common genetic background. B6. SJL-Ptprca Pepcb/BoyJ (CD45.1+) and *B6.129P2-Tcrb*^{tm1Mom} *Tcrd*^{tm1Mom}*/J* (β-/δ-TCR.Tg) mice were obtained from Jax, Inc. and bred within the animal facilities at University of Washington and Seattle Children's Research Institute.

Model of Mtb aerosol infection

Aerosol infections were performed with Mtb, H37Rv strain transfected with a mCherry reporter plasmid, described previously[33]. Mice were enclosed in a Glas-Col aerosol infection chamber and ~50–100 CFU were deposited into mouse lungs. Doses were confirmed using control mice by plating lung homogenates on 7H10 agar immediately after aerosol infection. Mice were sacrificed at indicated timepoint, and lungs were gently homogenized in PBS-containing 0.05%Tween using a gentleMacs dissociator (Miltenyi Biotec). Tissue homogenates were serially diluted on 7H10 agar and lung CFU was enumerated.

Flow Cytometry

Lung single cell suspensions were washed and stained for viability with Zombie Aqua viability dye (BioLegend) for 10 min at room temperature in the dark. After incubation, 100 μl of a surface antibody cocktail diluted in 50% FACS buffer/50% 24G2 Fc block buffer was added, and surface stains incubated for 30 min at 4°C. Antibodies are listed in Supplementary Table 1. The cells were washed once with FACS buffer and fixed with 2% paraformaldehyde for 1 h prior to analyzing on an LSRII or Symphony A3 flow cytometer (BD Biosciences). In some experiments, intracellular staining was performed after surface staining. Permeabilization was performed with Fix-Perm buffer (eBiosciences) for minimum of 60 min before the addition of intracellular antibodies. Then cells were fixed with 2% paraformaldehyde for 1 h prior to analyzing on an LSRII or Symphony A3 flow cytometer (BD Biosciences). For RNA-seq sorting experiments, 28 days after infection, mice were sacrificed, and AM were sorted on a BD FACSAria in a BSL-3 facility for infected and uninfected populations. The samples were spun and stored −80° C in Trizol. Phosphorylated EIF2 (pEIF2) was measured by flow cytometry using a previously published protocol[44].

Briefly, lung suspensions were isolated as above but subsequently permeabilized in ice-cold 100% methanol for 10 min, followed by antibody staining as in other protocols.

Chimera generation

Tollip$^{-/-}$ mixed bone marrow chimeras were generated in the following manner: B6.SJL-Ptprca Pepcb/BoyJ (CD45.1+; Jax, Inc.) F1 mice were lethally irradiated (1000 cGy). 5–10×10^6 bone marrow cells comprised of a 1:1 mixture of CD3-depleted (Miltenyi Biotec) *Tollip*$^{-/-}$ (CD45.2+) and F1 generation of C57BL/6J (CD45.1+45.2+) bone marrow was provided intravenously. For full bone marrow chimera generation, *Tollip*$^{-/-}$ mice were irradiated, followed by hemopoietic reconstitution by adoptive transfer of 5–10×10^6 bone marrow cells via intravenous injection. T cell chimeric mice were generated by sublethally irradiating β-/δ-TCR.Tg mice (600Gy), then intravenously injecting bone marrow (5–10×10^6 cells) from either B6 or *Tollip*$^{-/-}$ mice. Mice were permitted 6 weeks' recovery for immune reconstitution for sublethal irradiation and 10 weeks after lethal irradiation.

Tissue preparation and evaluation

Mice were euthanized and lungs were gently homogenized in HEPES buffer containing Liberase Blendzyme 3 (70 μg/ml; Roche) and DNase I (30 μg/ml; Sigma-Aldrich) using a gentleMacs dissociator (Miltenyi Biotec). The lungs were then incubated for 30 min at 37°C and then further homogenized a second time. The homogenates were filtered through a 70 μm cell strainer, pelleted for RBC lysis with RBC lysing buffer (Thermo), and resuspended in FACS buffer (PBS containing 2.5% FBS and 0.1% NaN_3).To prepare organs for histology, lung sections were inflated to 15cm water pressure with 4% paraformaldehyde, fixed in the same solution, embedded in paraffin, and sliced into 4μm sections. For histopathological analysis, 4 μm sections were cut and stained using a standard H&E protocol. Brightfield 40X whole-slide scans were obtained using the Leica SCN400 F whole-slide scanner through collaboration with the University of Washington Center for Lung Biology Histology Core Facility. For subjective histological evaluations, qualitative metrics were recorded in a blinded fashion.

Confocal Microscopy

Lungs were removed and placed in a 1:3 ratio BD Cytofix:PBS solution for 24 hours at 4°C. Lungs were washed twice with PBS, then placed in 30% sucrose for 24 hours at 4°C prior to embedding in optimal cutting temperature compound (OCT) and rapid freezing in an ethanol and dry ice slurry. 20μm sections were generated with a cryostat, then blocked for 1 hour in buffer (1% normal mouse serum (NMS), 1% BSA, 0.3% Triton, in 0.1M Tris) and stained overnight with fluorescently conjugated antibodies at room temperature. Finally, coverslips were added with Fluoromount G mounting media (SouthernBiotech). Images were acquired on a Leica Stellaris8 confocal microscope.

Histocytometry

Histocytometry analysis was performed as previously described, with minor adjustments[66]. Confocal images were first corrected for fluorophore spillover using the Leica Channel Dye Separation module. Single color controls, were generated by combining fluorescently

conjugated antibodies with mounting media, mounting on slides, and imaging. The Imaris surface creation module was used to create cell objects around CD68+ signal. Detection of the brightest pEIF2 signal was facilitated by forming objects around this signal in the Imaris surface creation module, then setting the value of pEIF2 fluorescence outside of these objects to 0. CD68+ object statistics were then exported to Excel (Microsoft). Object statistics were concatenated into on CSV file per sample, then imported into FlowJo software for hierarchical gating and analysis. For visual clarity, presented images were manipulated in Imaris and PowerPoint (Microsoft), with identical manipulation applied across experimental groups.

Intracellular Mtb replication

Frozen Mtb was thawed and cultured on a shaking incubator for two doubling cycles. One day prior to infection, cultures were back-diluted into an optical density (OD) of 0.2–0.4 in 7H9 media supplemented with glycerol (4%), Middlebrook ADC Growth Supplement (100 mL/L), and Tween 80 (0.05%). At the time of infection, Mtb was filtered through a 5 μm syringe filter to remove bacterial clumps, and cells were inoculated at indicated MOI. The inoculum was prepared in RPMI-10 medium and applied to cells, which were centrifuged at 300g for 5 minutes and incubated for 4 hours at 37°C. Supernatants were removed and washed twice with prewarmed PBS to remove unbound bacteria, before adding per warmed RPMI supplemented with 10% FBS. Intracellular growth was determined using luminescence on a Synergy H4 multimode microplate reader (Biotek Instruments) daily from Day 0 to Day 3. In some experiments, 24hrs post infection cell culture supernatants were collected and filtered twice using 0.22μm filter and frozen at −80°C.

Macrophage preparation

Resident peritoneal cells, mainly consisting of *in vivo* differentiated macrophages, were isolated using standard methods. 10ml of cold PBS were injected intraperitoneally using a 27g needle, and the peritoneum was gently messaged. Cells were removed with PBS, centrifuged at 4° C at 300g, and placed into warm RPMI media. PEMs (1×10^5/well) were plated in 96-well plates in 200μL of antibiotic-free RPMI 1640 containing with 10% Fetal Bovine Serum (Atlas Biologics). Cells were rested for minimum 24hrs before further experimentation. Bone marrow was harvested from mice and grown in RPMI supplemented with 10% heat inactivated FBS and M-CSF (40ng/ml) in tissue culture treated plates. Cells were then incubated at 37° C for 6 to 7 days. Bone marrow-derived macrophages (BMDM) were used after 7 days of culture. BMDMs were detached by gentle scraping and were then plated in RPMI 1640 supplemented with 10% heat inactivated FBS. Alveolar macrophages (AM) were isolated by bronchoalveolar lavage (BAL) with 9 mL PBS supplemented with 1mM EDTA on mice euthanized with ketamine as previously described[67]. The lavage was centrifuged at 300g for 5 minutes and resuspended in RPMI supplemented with 10% FBS. AM purity was analyzed by flow cytometry and confirmed to be greater than 95%. For *in vitro* experiments, AMs were pulsed with penicillin and streptomycin for four hours prior to stimulation. For adoptive transfer experiments, recipient mice were treated with 50μl clodronate-loaded liposomes via the oropharyngeal route 72 hr before adoptive transfer to deplete AMs and provide a permissive niche for engraftment. Donor AM (2×10^5 cells in

50μl PBS) were transferred into clodronate-conditioned mice immediately after isolation via intratracheal instillation into isoflurane-anesthetized mice.

Gene editing

Guide RNA was constructed for TOLLIP (primer sequence GGAGGTGATCCGCTCCGTGC) using https://chopchop.rc.fas.harvard.edu/ [68]. The guide RNA and a scaffold connecting Cas9 endonuclease to the sequence of interest were cloned into an empty gRNA-Cas9-t2a-puromycin pRRL lentiviral plasmid using the Clontech InFusion system (Takara Bio, Inc.). Subsequently, plasmids were inserted into Stellar Competent Cells per the InFusion kit protocol. Colonies were screened on LB plates with ampicillin. Plasmids were then confirmed using sequencing. Lentivirus was produced in HEK293T Lenti-X cells at a passage number less than 10 by transfecting TOLLIP-pRRL plasmid with the plasmids pRSV-Rev, pMD2.g, and pMDLg/pRRe, in Opti-MEM and TransiT-LT1 (Mirius Bio, Inc.). After 24 hours' incubation, media was replaced with fresh, warm RPMI with 10% FBS and were incubated for another 24 hours. Supernatants were filtered through a 0.45μm filter and incubated with recipient THP-1 cells in media with 5μg/ml polybrene supplementation. Transduced THP-1 cells were allowed to rest for 24 hours in fresh media after incubation with lentiviral particles. THP-1 cells underwent selection in 5μg/ml puromycin for three days. Remaining cells were sequenced, and Western blot was performed to confirm frameshift insertion and protein knockout (data not shown).

Mycolic acid preparation

Synthetic α-mycolic acid (C80) in a mixture of three isoforms (alpha, keto, hydroxy) in equal measure was obtained from Avanti Polar Lipids. Powdered lipids were solubilized in chloroform, which was evaporated in the plate and the lipids recovered in RPMI with 10% FBS. The suspension was sonicated at 37°C for 20 min, followed by addition of cells. Control suspensions were prepared similarly but without the addition of MA and sonicated before administration. 50μg of mycolic acid were administered to cells of interest for 72 hours prior to measurement, as previously described [29]. MA was free from endotoxin as determined by a chromogenic Limulus amebocyte lysate assay (Genscript).

Cellular Studies

Cell-culture supernatants were collected at indicated time and frozen at −20 °C until analysis. The cytokine concentrations in the culture supernatant were determined using quantitative ELISA (Mouse TNF and IL-10 DuoSet; R&D Systems) as recommended by the manufacturer. For detection of lipid bodies, macrophages were plated (1×10^5/well) in a glass bottomed chamber slide. Cells were washed twice and resuspended in PBS solution of HCS LipidTOX Deep Red Neutral Lipid stain (ThermoFisher Scientific) according to manufacturer instruction. After incubation, cells were washed twice with PBS and fixed in 2% PFA for 30min. Cells were mounted in medium containing DAPI stain (ProLong Gold, Thermo, Inc.). Lipid droplets were counted from 100 cells identified randomly selected high-powered fields.

Western blotting

5–20μg of cell or tissue protein extract was separated by SDS-PAGE, transferred onto PVDF membranes, and immunoblotted with primary antibodies listed in Supplementary Table 1. Secondary antibodies conjugated to horseradish peroxidase were added and luminescence was quantitated using Signalfire ECL reagent (Cell Signaling).

Preparation of total RNA and sequencing

Total RNA from sorted cells was isolated using the manufacturer's instructions (TRIzol, Invitrogen). The RNA purity and quantified was assessed by RNA-Tapestation (Agilent 4200). cDNA was prepared using SMART-Seq v4 Ultra Low Input RNA Kit (Takara Bio USA, Inc). RNA sequencing libraries were prepared using the Illumina TruSeq™ RNA Sample Preparation Kit (Illumina, San Diego, CA, USA). Samples were sequenced as 50 bp paired-end reads on a Illumina HiSeq 2500 and assessed using FastQC v0.11.8 to visualize sequence quality. Sequences were filtered using AdapterRemoval v2.3.1 to remove adapters, remove sequences with >1 ambiguous base, and trim ends to a 30+ Phred score. Sequences were aligned to the mouse genome mm10 using STAR v2.7.4a, and alignments were assessed with Picard v2.18.7 and samtools v1.10. Total reads in gene exons were quantified using featureCounts v2.0.1.

Differential expression analysis

Gene expression analyses were performed in R v3.6.1 with the tidyverse v1.3.0 [69]. Overall, samples were very high-quality with > 32 million aligned sequences per sample and low variability in gene coverage (median coefficient of variation coverage < 0.6). Genes were filtered to protein coding genes with biomaRt (N = 21850) with > 0.1 counts per million (CPM) in at least three samples (N = 14215) [70]. Counts were normalized for RNA composition using edgeR and log2 CPM voom normalized with quality weights using limma[71, 72]. Differentially expressed genes were determined using limma using a contrasts model comparing B6 and *Tollip*$^{-/-}$ cells in uninfected and infected groups (**Table S2**). Genes with FDR < 0.05 for at least one contrast (N = 294) were included in Ingenuity Pathway analysis. The Benjamini–Hochberg correction for multiple comparisons was applied to P-values and significance was assessed at FDR < 0.05 for all tests.

Statistics

All mouse numbers are shown in figure legends. No data were excluded from this study. Cellular measurements were compared using a two-sided *t*-test unless otherwise specified in the figure legend. A value of $p < 0.05$ was considered a statistically significant result unless otherwise specified. Statistics were calculated using Prism version 10.1 (GraphPad, Inc.).

Extended Data

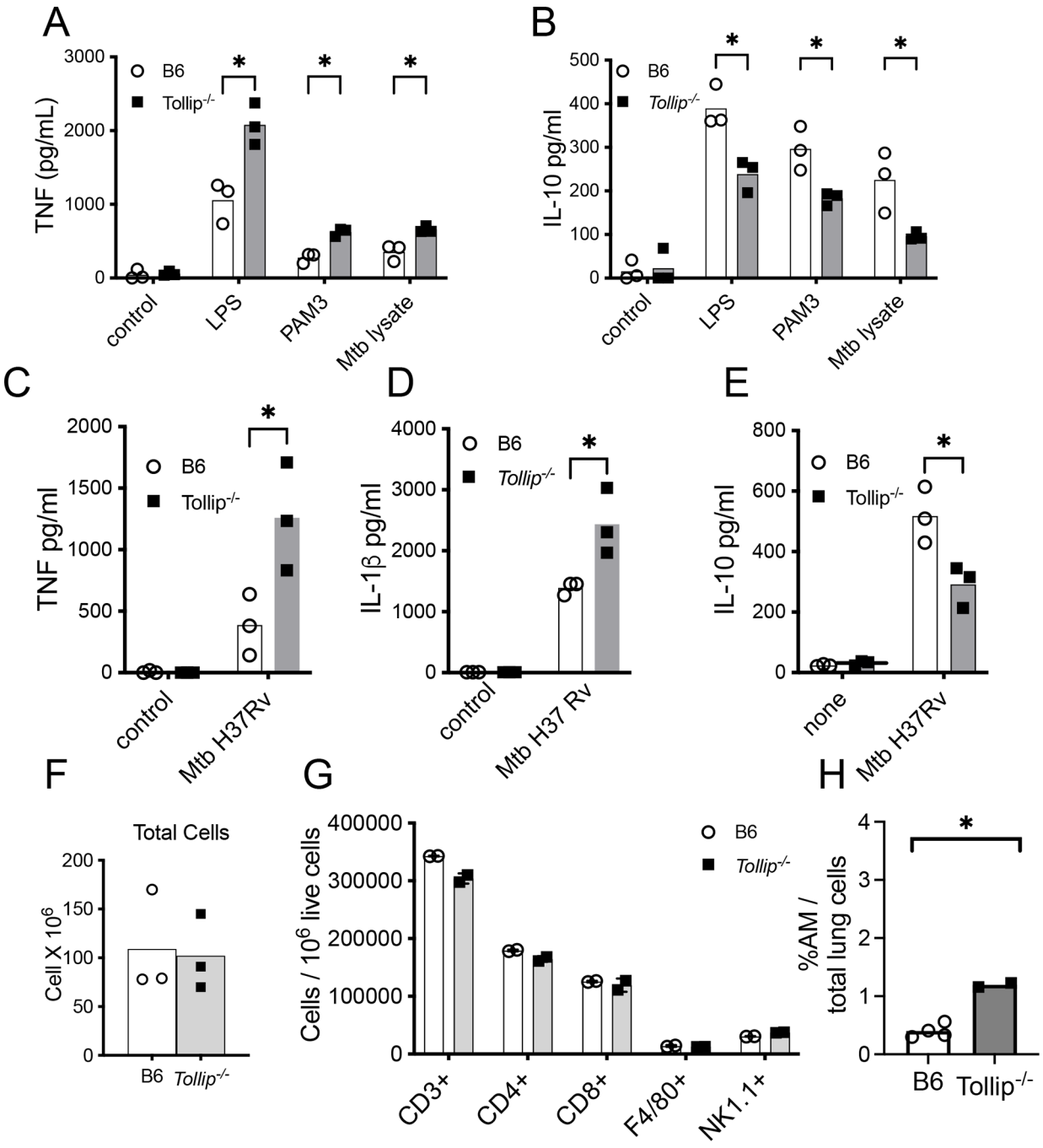

Extended Data 1. *Tollip*$^{-/-}$ macrophages are hyperinflammatory.

A-B) Peritoneal extract macrophages (PEM) were isolated from *Tollip*$^{-/-}$ and B6 mice, plated, stimulated with control (Uns), LPS (10ng/ml), PAM3 (250ng/ml), or Mtb whole cell lysate (1μg/ml) overnight and **A)** TNF and **B)** IL-10 were measured from cellular supernatants by ELISA.**C-E)** PEM were infected with Mtb H37Rv strain (MOI 2.5) overnight *ex vivo*, then **C)** TNF, **D)** IL-1β, and **E)** IL-10 were measured from cellular

supernatants by ELISA. **F-H)** Baseline immune cell number in *Tollip*$^{-/-}$ mice. Total number of **F)** splenocytes, **G)** CD3+, C4+ CD8+, F4/80+, and NK1.1+ splenocytes, and the **H)** proportion of alveolar macrophages (AM) in the lungs of healthy 8-week-old mice, measured by flow cytometry. N = 3 measurements per experiment; each experiment was performed twice. * p<0.05, student's two sided t-test.

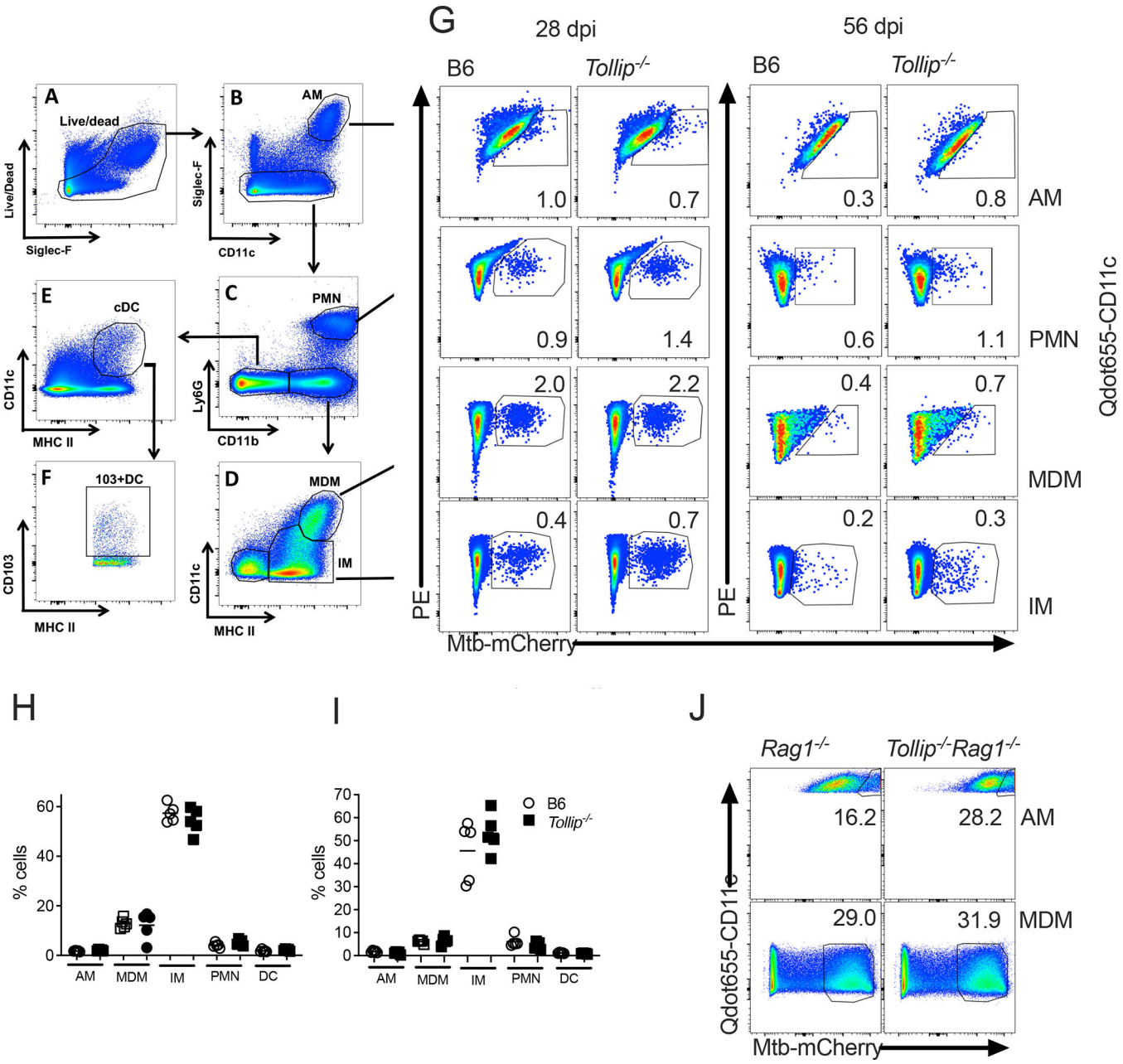

Extended Data 2. Related to Figure 1. Characteristics of Mtb-infected *Tollip*$^{-/-}$ lungs.

A-G) Gating strategy used to identify Mtb-infected lung-resident myeloid cell subsets. **A)** Live/Dead Fixability dye was used to exclude dead cells, **B)** AM were identified by coexpression of SiglecF and CD11c. **C)** SiglecF− cells were gated; CD11b+Ly6G+ cells

were classified as neutrophils, and CD11b+Ly6G− cells were considered macrophages. **D)** MHC-II+CD11c+ macrophages were subclassified as monocyte-derived macrophage cells (MDM) and MHC-II+CD11c− as interstitial macrophages (IM). **E)** CD11b-Ly6G− cells were gated and MHC-II+CD11c+ cells were classified as conventional DC (cDC) or **F)** CD103+ cDC) was measured. **G)** Representative flow cytometry images of the proportion of Mtb-infected myeloid subsets 28 and 56 days post infection (dpi).
H-I) Proportion of total alveolar macrophages (AM), monocyte-derived macrophages (MDM), interstitial macrophages (IM), neutrophils (PMN), and dendritic cells (DC) in Mtb-infected mice **H)** 28 and **I)** 56 days after infection; n= 10; two-sided t-test.
J) Representative flow cytometry images of Mtb-mCherry expression in AM and MDM from *Rag1*$^{-/-}$ and *Tollip*$^{-/-}$*Rag1*$^{-/-}$ mice 28 days after infection.

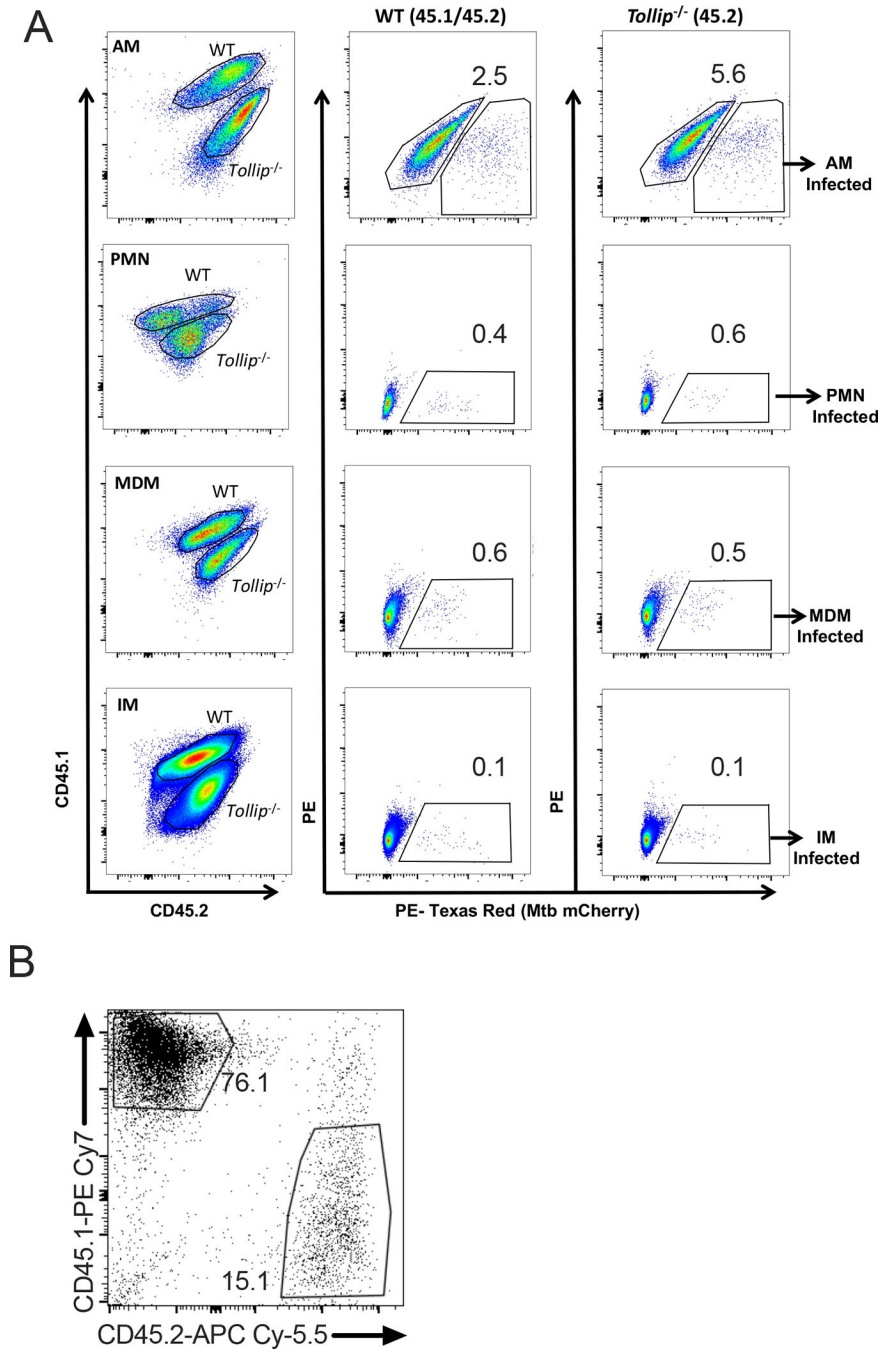

Extended Data 3. Related to Figure 2. Gating strategy used to identify lung-resident myeloid cells in mixed bone marrow chimeric mice.

A-D) Mixed bone marrow chimeric mice were infected with Mtb H37Rv expressing mCherry reporter plasmid (Mtb-mCherry) (50–100 CFU) via aerosol. At selected time points flow analysis was performed to identify populations infected with Mtb. Myeloid populations were identified as in Extended Data 2. **A) Alveolar macrophages** (AM), neutrophils (PMN), monocyte-derived macrophages (MDM), andinterstitial macrophages (IM) were subclassified as B6 or *Tollip*$^{-/-}$ based on CD45.1/CD45.2 or CD45.2 expression,

respectively, and the proportion of mCherry-Mtb cells measured. Representative images from 28 days post infection are shown.

E) Representative image of CD45.2+ *Tollip*$^{-/-}$ AM adoptively transferred into CD45.1+ mice 56 days after AM depletion.

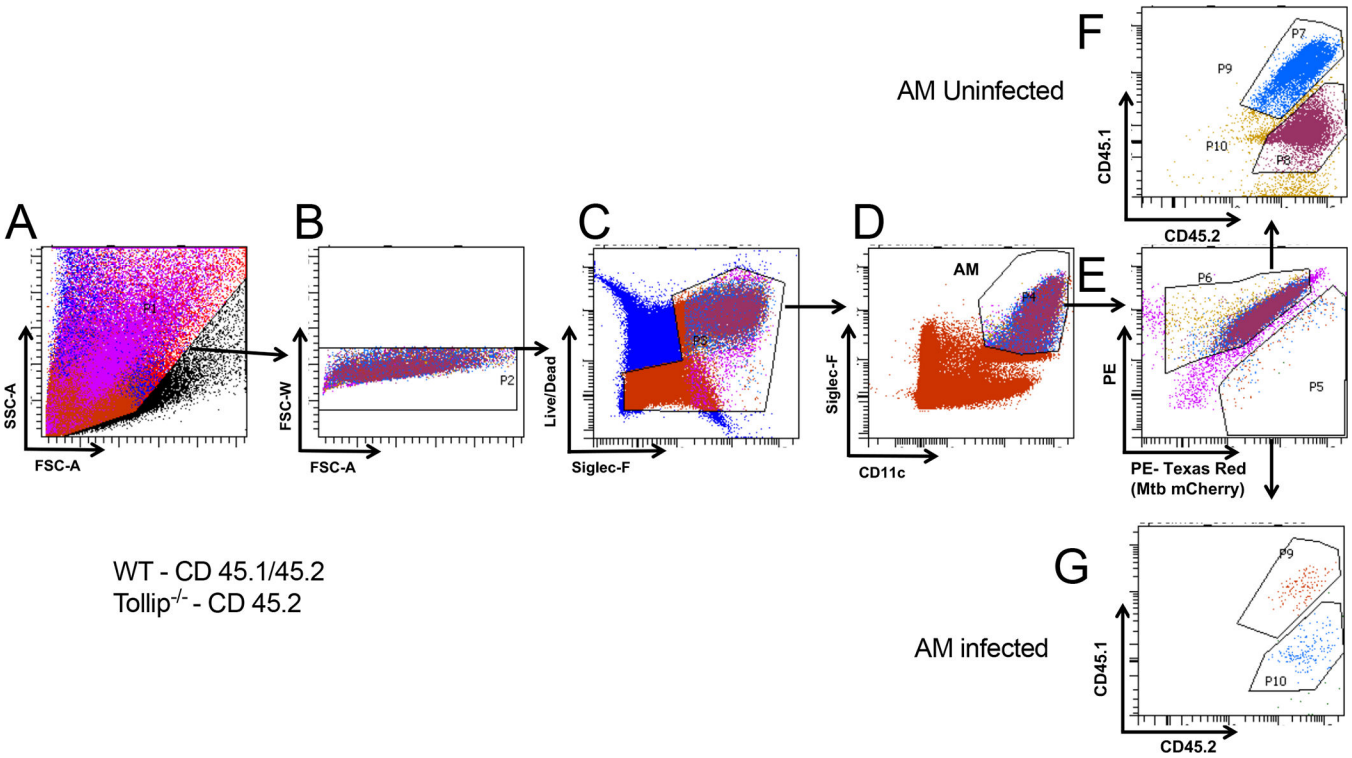

Extended Data 4. Related to Figure 3. Gating strategy used for sorting Mtb-infected AM.

Mixed bone marrow mice were infected with Mtb H37Rv (50–100 CFU) via aerosol and AM were sorted for RNA seq analysis 28 days post infection, from *left* to *right*. **A)** Lymphocyte gating, followed by **B)** Singlet identification. **C)** Live/Dead Fixability dye was used to exclude dead/dying cells, and **D)** SiglecF+ CD11c+ cells were classified as AM. **E)** Uninfected and Mtb-infected AM were identified by mCherry expression **F)** Uninfected AM and **G)** Mtb-infected AM genetic lineage was defined based on CD45.1/CD45.2 (F1 B6) or CD45.2 (*Tollip*$^{-/-}$) expression, respectively.

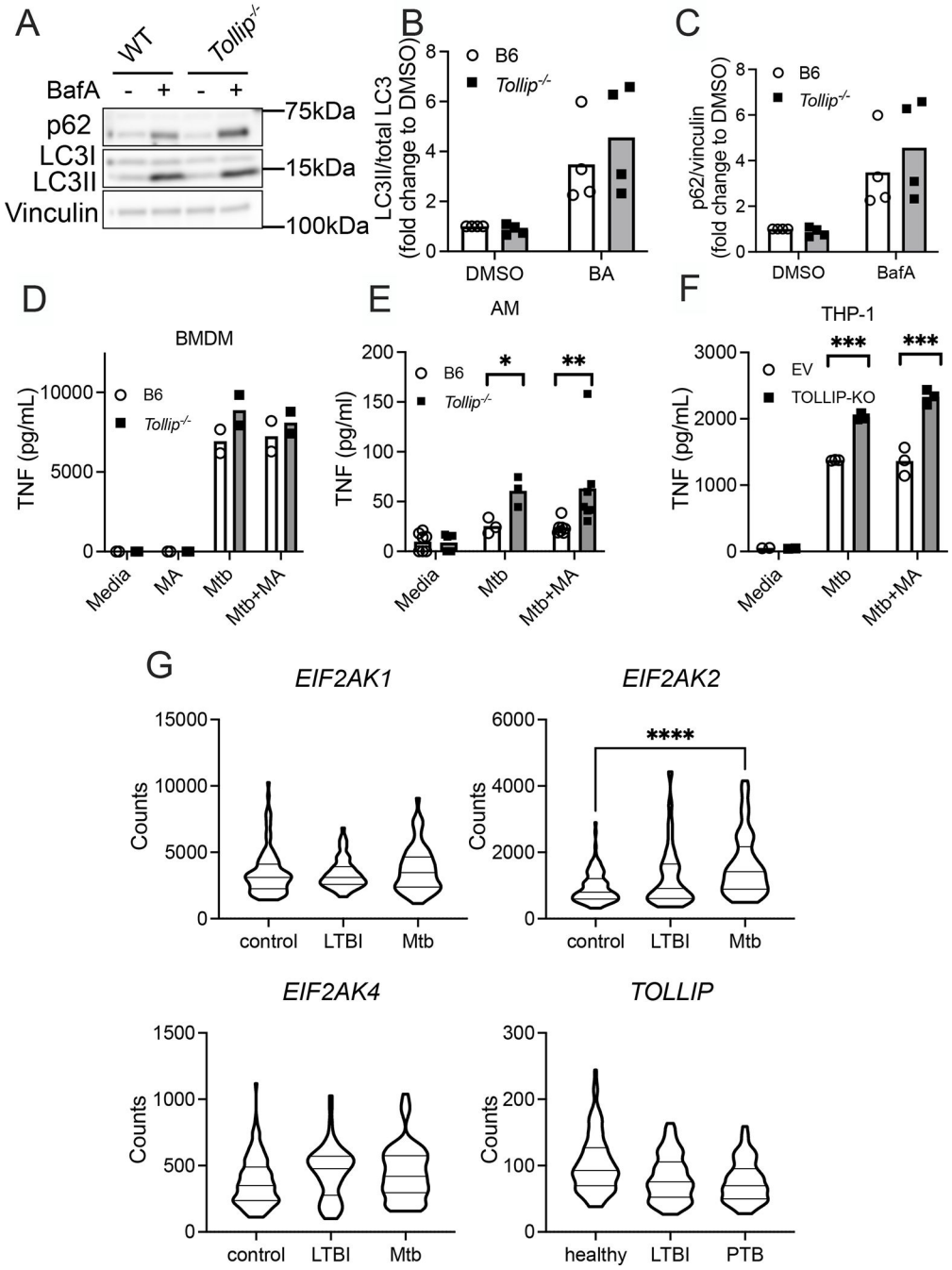

Extended Data 5. Related to Figure 4. Tollip is dispensable for bulk autophagy in macrophages.

Bone marrow from B6 (*white* bars) or *Tollip*$^{-/-}$ (*black* bars) were differentiated *ex vivo* to macrophages using 40ng/mL M-CSF for 7–9 days. Following differentiation, BMDMs were treated for 6hr with or without 250nM Bafilomycin A (BafA). **A)** Representative western blot results showing protein levels of LC3I/II and p62.

B) Quantification of protein levels (by densitometry) of LC3II using total LC3 (I+II) as a loading control. ***p<0.001 2-way ANOVA for an effect of BafA.

C) Quantification of p62 levels (by densitometry) using vinculin as a loading control. p=0.056 2-way ANOVA effect of BafA.
D-F) TNF concentrations in the supernatants of TOLLIP-deficient **D)** BMDM, **E)** alveolar macrophages (p=0.02 between genotypes in Mtb and p=0.03 in MA+Mtb groups; AM), and **F)** THP-1 cells 24 hours after Mtb infection (MOI 5) and mycolic acid (MA; 10μg/ml) treatment by ELISA (p=0.0002 between genotypes in Mtb and p<0.0001 in MA+Mtb groups; AM)* p < 0.05, ** p<0.01, *** p<0.001, two-sided t-test. Experiment was performed in BMDM twice and all other cell types three times.
G) Expression of *EIF2AK1*, *EIF2AK2*, *EIF2AK4*, and *TOLLIP* in human whole blood in heathy controls (control) or patients with latent tuberculosis infection (LTBI), active symptomatic pulmonary TB disease (Mtb). *EIF2AK3* was not detected in this dataset. Data are shown as violin plots with lines indicating 25th, 50th, and 75th percentile, extending to minimum and maximum value. Obtained from GSE 19491[53].

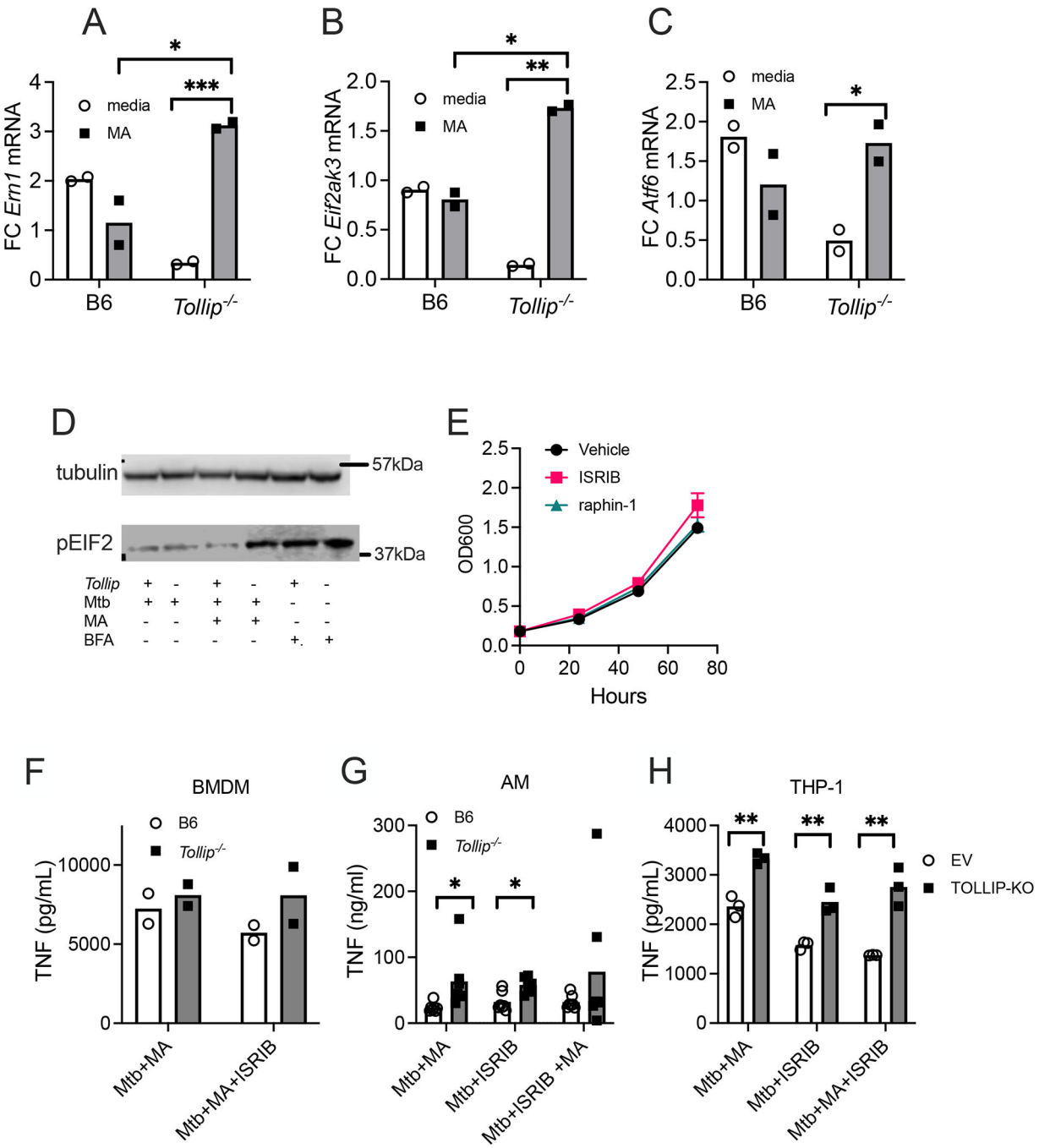

Extended Data 6. Related to Figure 6. Evaluation of integrated stress responses in *Tollip*$^{-/-}$ mice and macrophages

A-C) B6 and *Tollip*$^{-/-}$ peritoneal extract macrophages (PEM) were incubated with media or mycolic acid (MA; 10μg/ml) for 72 hours, then infected with Mtb (MOI 1) overnight. mRNA transcripts of key regulatory genes of the cellular stress response were measured before and after Mtb infection. **A)** *Ern1* (IRE1a; p = 0.001 for media, p= 0.049 for MA), **B)** *Eif2ak3* (PERK; p = 0.002 for media, p= 0.007 for MA), and **C)** *Atf6* (ATF6; p = 0.02 for media) were measured and displayed as their fold change from baseline after Mtb

infection. FC = (Normalized mRNA expression after Mtb infection) / (Normalized mRNA expression after media control stimulation). N=2/group and are representative of at least two independent experiments.

D) Western blot of PEM incubated as above measuring pEIF2 and tubulin expression.

E) Optical density at 600nm (OD600) of Mtb H37Rv in 7H9 broth culture in the presence of raphin-1 (10 μM), ISRIB (250 nM), or vehicle control over time. N = 2 over two independent experiments; error bars – SEM.

F-H) TNF concentrations in cellular supernatants from TOLLIP-deficient **F)** bone marrow-derived macrophages (BMDM), **G)** alveolar macrophages (AM; p = 0.04 for Mtb+MA, p=0.003 for Mtb+ISRIB) and **H)** THP-1 cells (p = 0.002 for Mtb+MA, p=0.005 for Mtb+ISRIB, p=0.004 for Mtb+MA+ISRIB), after 24 hours of Mtb infection (MOI 5), mycolic acid (MA, 10μg/ml), and ISRIB (250nM), measured by ELISA. This experiment was performed twice, each with three technical replicates. * $p < 0.05$, ** $p < 0.01$, two-sided t-test.

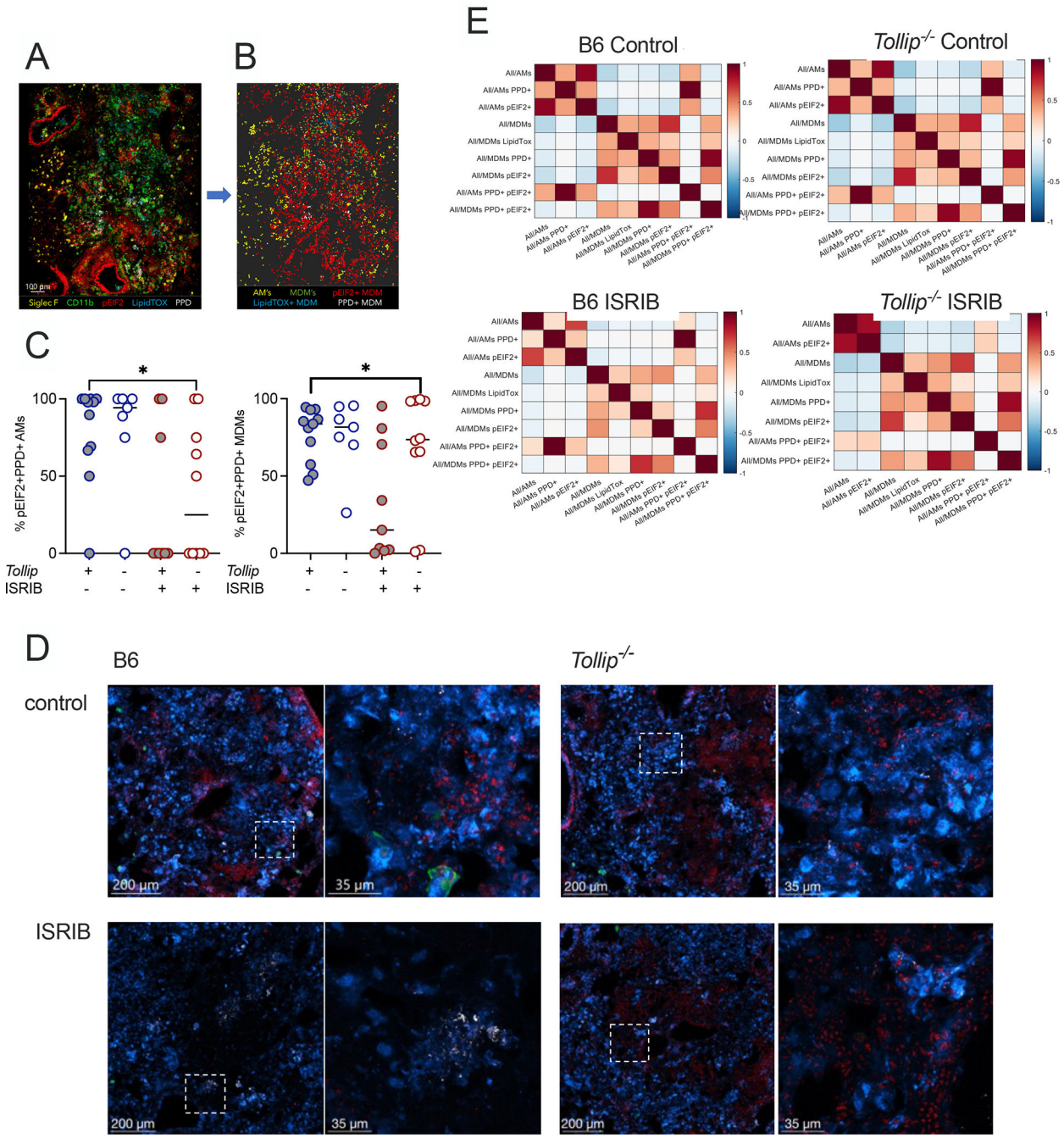

Extended Data 7. Images related to Figure 6 histocytometry studies.

A) Representative confocal microscopy image of the lungs of a B6 mouse infected with Mtb for 56 days. *Yellow* – SiglecF; *green* – CD11b; *red* – pEIF2; *blue* – LipidTox; *white* --- PPD. **B)** Histocytometry positional mapping of AM and MDM within the Mtb-infected lung. **C)** Proportion of pEIF2+ PPD+ AM (p = 0.017 for overall ANOVA effect) and MDM (p = 0.016 for overall ANOVA effect) in B6 and *Tollip*$^{-/-}$ mice at baseline and after ISRIB treatment. p = 0.02 for overall ANOVA effect. * p<0.05, one-sided ANOVA. N = 4 B6

control mice, N = 5 B6 ISRIB mice, N = 6 *Tollip*$^{-/-}$ control, and N = 6 *Tollip*$^{-/-}$ ISRIB mice.

D) Representative images staining from the lungs of Mtb-infected B6 and *Tollip*$^{-/-}$ mice with and without ISRIB treatment. *Red* -- pEIF2; *green* -- CD68; *blue* – SiglecF; *white* -- PPD.

E) Spatial correlation analysis of cell types within 20-mm-radius neighborhoods in B6 and *Tollip*$^{-/-}$ mice. Red shades indicate positive correlation, and blue shades indicate negative correlation.

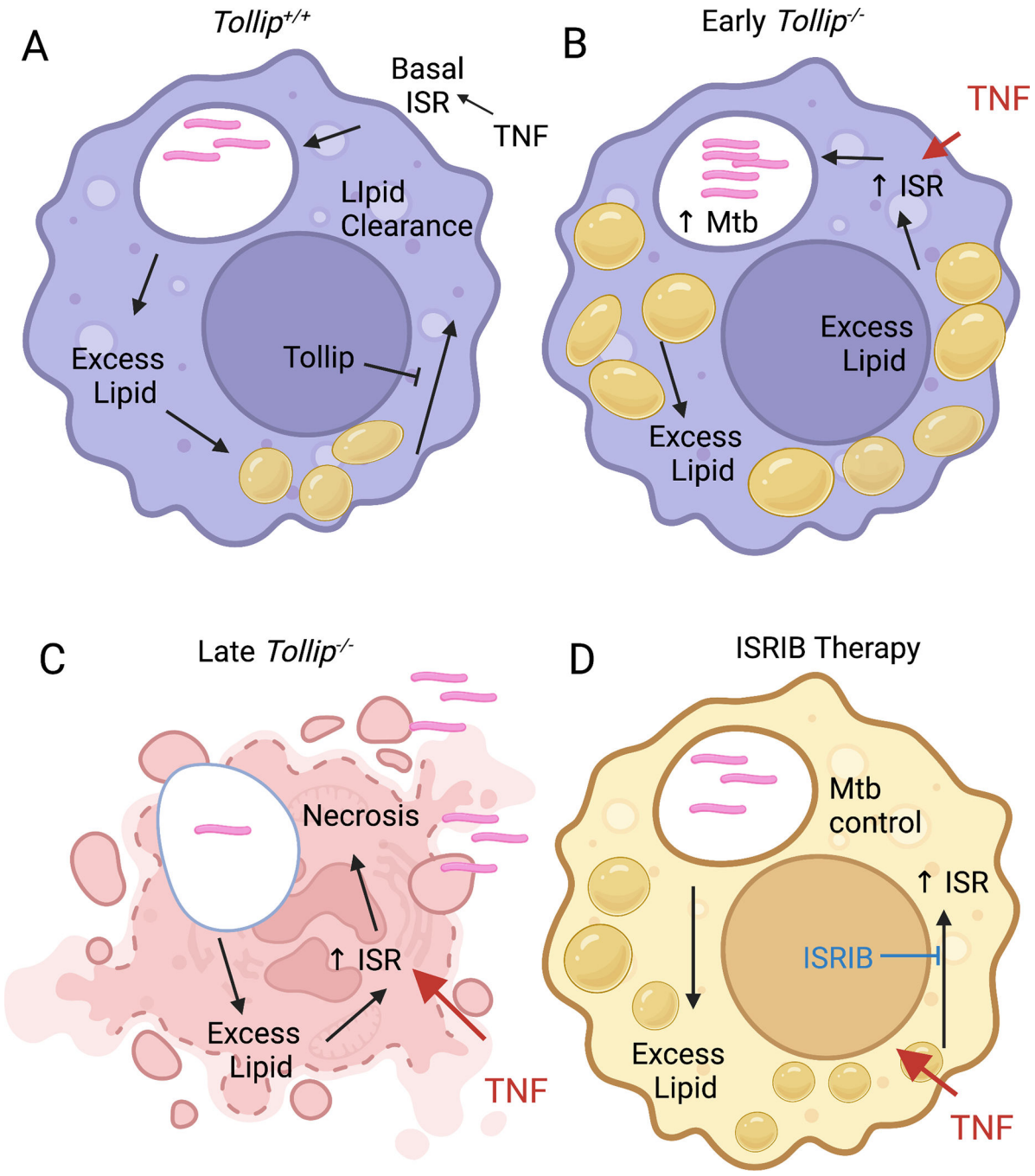

Extended Data 8. Overall experimental model

. A) Basal homeostasis. During chronic Mtb infection, lipid products are released in Mtb-infected AM. TOLLIP prevents lipid accumulation and controls inflammation, which maintains EIF2 signaling at a basal level.

B) *Tollip*$^{-/-}$ AM. *Tollip*$^{-/-}$ mice develop excess TNF and IFNα responses from macrophages and T cells. Mtb-infected *Tollip*$^{-/-}$ AM undergo lipid accumulation, which increases EIF2 phosphorylation. Excess pEIF2 induces sensitivity to inflammation in AM.

C) Chronic infection in *Tollip*$^{-/-}$ AM. During prolonged infection, increased and prolonged EIF2 phosphorylation from lipids and inflammation leads to cellular necrosis, decreasing the Mtb burden within individual AM and releasing extracellular Mtb.

D) ISRIB treatment. ISRIB improves AM host defense, which improves Mtb control in both B6 and *Tollip*$^{-/-}$ mouse models, making it an effective therapeutic across genetic backgrounds.

Supplementary Material

Refer to Web version on PubMed Central for supplementary material.

Acknowledgments

The authors wish to thank the University of Washington Center for Lung Biology Histology and Imaging Core for their helpful advice on pathology staining and analysis. We are grateful to the Seattle Children's Research Institute Cell Sorting Core for their assistance and technical support. Flow cytometry data was acquired through the University of Washington, Cell Analysis Facility Shared Resource Lab, with NIH award 1S10 OD024979–01A1. We thank Lalita Ramakrishnan for helpful conversations and Michelle Sabo for copy editing. Funding: This work was supported by the NIH (R01 AI136912 to JAS; R01 DK108921 to SAS) and the Department of Veterans Affairs (I01 BX004444 to SAS). GLP was supported by the American Diabetes Association (19-PDF-063).

Data Availability

Datasets generated in this study are available in Source data. Image data is available at Zenodo.org; doi:10.5281/zenodo.10475042. All sequencing data that support the findings of this study have been deposited in the National Center for Biotechnology Information Gene Expression Omnibus (GEO) and are accessible through the GEO Series accession number GSE243818. Any other relevant data are available from the corresponding author on request.

References

1. Shah JA et al. Human TOLLIP Regulates TLR2 and TLR4 Signaling and Its Polymorphisms Are Associated with Susceptibility to Tuberculosis. J Immunol 189, 1737–1746 (2012). [PubMed: 22778396]
2. Shah JA et al. A Functional TOLLIP Variant is Associated with BCG-Specific Immune Responses and Tuberculosis. Am J Respir Crit Care Med (2017).
3. Shah JA et al. Genetic Variation in Toll-Interacting Protein Is Associated With Leprosy Susceptibility and Cutaneous Expression of Interleukin 1 Receptor Antagonist. J Infect Dis 213, 1189–1197 (2016). [PubMed: 26610735]
4. Uhlén M et al. Proteomics. Tissue-based map of the human proteome. Science 347, 1260419 (2015). [PubMed: 25613900]
5. Jongsma ML et al. An ER-Associated Pathway Defines Endosomal Architecture for Controlled Cargo Transport. Cell 166, 152–166 (2016). [PubMed: 27368102]
6. Chen K, Yuan R, Zhang Y, Geng S & Li L Tollip Deficiency Alters Atherosclerosis and Steatosis by Disrupting Lipophagy. J Am Heart Assoc 6, e004078 (2017). [PubMed: 28396568]
7. Lu K, Psakhye I & Jentsch S Autophagic clearance of polyQ proteins mediated by ubiquitin-Atg8 adaptors of the conserved CUET protein family. Cell 158, 549–563 (2014). [PubMed: 25042851]
8. Shah JA et al. TOLLIP deficiency is associated with increased resistance to Legionella pneumophila pneumonia. Mucosal Immunol 12, 1382–1390 (2019). [PubMed: 31462698]
9. Burns K et al. Tollip, a new component of the IL-1RI pathway, links IRAK to the IL-1 receptor. Nat Cell Biol 2, 346–351 (2000). [PubMed: 10854325]

10. Ryan TA et al. Tollip coordinates Parkin-dependent trafficking of mitochondrial-derived vesicles. Embo J 39, e102539 (2020). [PubMed: 32311122]
11. Zellner S, Schifferer M & Behrends C Systematically defining selective autophagy receptor-specific cargo using autophagosome content profiling. Mol Cell (2021).
12. Zhang G, Ghosh S Negative Regulation of Toll-like Receptor-mediated Signaling by Tollip. Journal of Biological Chemistry 277, 7059–7065 (2002). [PubMed: 11751856]
13. Brissoni B et al. Intracellular trafficking of interieukin-1 receptor I requires Tollip. Curr. Biol. 16, 2265–2270 (2006). [PubMed: 17113392]
14. Pokatayev V et al. Homeostatic regulation of STING protein at the resting state by stabilizer TOLLIP. Nat Immunol 21, 158–167 (2020). [PubMed: 31932809]
15. Kowalski EJA & Li L Toll-Interacting Protein in Resolving and Non-Resolving Inflammation. Front Immunol 8, 511 (2017). [PubMed: 28529512]
16. Noth I et al. Genetic variants associated with idiopathic pulmonary fibrosis susceptibility and mortality: a genome-wide association study. Lancet Respir Medicine 1, 309–317 (2013).
17. Li M et al. Tollip is a critical mediator of cerebral ischaemia–reperfusion injury. J Pathology 237, 249–262 (2015).
18. Zhi H et al. Tollip Negatively Regulates Vascular Smooth Muscle Cell–Mediated Neointima Formation by Suppressing Akt-Dependent Signaling. J Am Heart Assoc 7 (2018).
19. Behar SM et al. Apoptosis is an innate defense function of macrophages against Mycobacterium tuberculosis. Mucosal immunology 4, 279 287 (2011). [PubMed: 21307848]
20. Roca FJ & Ramakrishnan L TNF dually mediates resistance and susceptibility to mycobacteria via mitochondrial reactive oxygen species. Cell 153, 521–534 (2013). [PubMed: 23582643]
21. Berg RD et al. Lysosomal Disorders Drive Susceptibility to Tuberculosis by Compromising Macrophage Migration. Cell 165, 139–152 (2016). [PubMed: 27015311]
22. Tzelepis F et al. Mitochondrial cyclophilin D regulates T cell metabolic responses and disease tolerance to tuberculosis. Sci Immunol 3, eaar4135 (2018). [PubMed: 29752301]
23. Feng CG et al. Mice lacking myeloid differentiation factor 88 display profound defects in host resistance and immune responses to Mycobacterium avium infection not exhibited by Toll-like receptor 2 (TLR2)− and TLR4-deficient animals. J Immunol 171, 4758–4764 (2003). [PubMed: 14568952]
24. Bafica A et al. TLR9 regulates Th1 responses and cooperates with TLR2 in mediating optimal resistance to Mycobacterium tuberculosis. Journal of Experimental Medicine 202, 1715–1724 (2005). [PubMed: 16365150]
25. Watson RO et al. The Cytosolic Sensor cGAS Detects Mycobacterium tuberculosis DNA to Induce Type I Interferons and Activate Autophagy. Cell Host Microbe 17, 811–819 (2015). [PubMed: 26048136]
26. Philips JA, Porto MC, Wang H, Rubin EJ & Perrimon N ESCRT factors restrict mycobacterial growth. Proceedings of the National Academy of Sciences of the United States of America 105, 3070–3075 (2008). [PubMed: 18287038]
27. Roca FJ, Whitworth LJ, Redmond S, Jones AA & Ramakrishnan L TNF Induces Pathogenic Programmed Macrophage Necrosis in Tuberculosis through a Mitochondrial-Lysosomal-Endoplasmic Reticulum Circuit. Cell 178, 1344–1361 e1311 (2019). [PubMed: 31474371]
28. Lovewell RR, Sassetti CM & VanderVen BC Chewing the fat: lipid metabolism and homeostasis during M. tuberculosis infection. Curr Opin Microbiol 29, 30–36 (2016). [PubMed: 26544033]
29. Peyron P et al. Foamy macrophages from tuberculous patients' granulomas constitute a nutrient-rich reservoir for M. tuberculosis persistence. PLoS Pathog 4, e1000204 (2008). [PubMed: 19002241]
30. Lo YLS, Beckhouse AG, Boulus SL & Wells CA Diversification of TOLLIP isoforms in mouse and man. Mammalian Genome 20, 305–314 (2009). [PubMed: 19444506]
31. Russell DG, Huang L & VanderVen BC Immunometabolism at the interface between macrophages and pathogens. Nat Rev Immunol 19, 291–304 (2019). [PubMed: 30679807]

32. Guilliams M et al. Alveolar macrophages develop from fetal monocytes that differentiate into long-lived cells in the first week of life via GM-CSF. J Exp Med 210, 1977–1992 (2013). [PubMed: 24043763]
33. Cohen SB et al. Alveolar Macrophages Provide an Early Mycobacterium tuberculosis Niche and Initiate Dissemination. Cell Host Microbe 24, 439–446 e434 (2018). [PubMed: 30146391]
34. Moguche AO et al. ICOS and Bcl6-dependent pathways maintain a CD4 T cell population with memory-like properties during tuberculosis. J Exp Medicine 212, 715–728 (2015).
35. Consortium GT Human genomics. The Genotype-Tissue Expression (GTEx) pilot analysis: multitissue gene regulation in humans. Science 348, 648–660 (2015). [PubMed: 25954001]
36. Moguche AO et al. ICOS and Bcl6-dependent pathways maintain a CD4 T cell population with memory-like properties during tuberculosis. J Exp Med 212, 715–728 (2015). [PubMed: 25918344]
37. Nwosu ZC, Ebert MP, Dooley S & Meyer C Caveolin-1 in the regulation of cell metabolism: a cancer perspective. Molecular Cancer 15, 71 (2016). [PubMed: 27852311]
38. Stutz MD et al. Macrophage and neutrophil death programs differentially confer resistance to tuberculosis. Immunity 54, 1758–1771 e1757 (2021). [PubMed: 34256013]
39. Joshi N, Walter JM & Misharin AV Alveolar Macrophages. Cellular Immunology 330, 86–90 (2018). [PubMed: 29370889]
40. Lavin Y, Mortha A, Rahman A & Merad M Regulation of macrophage development and function in peripheral tissues. Nature Reviews Immunology 15, 731–744 (2015).
41. Krämer A, Green J, Pollard J Jr. & Tugendreich S Causal analysis approaches in Ingenuity Pathway Analysis. Bioinformatics 30, 523–530 (2014). [PubMed: 24336805]
42. Gillespie M et al. The reactome pathway knowledgebase 2022. Nucleic Acids Research 50, D687–D692 (2022). [PubMed: 34788843]
43. Hinnebusch AG Mechanism and regulation of initiator methionyl-tRNA binding to ribosomes. COLD SPRING HARBOR MONOGRAPH SERIES 39, 185–244 (2000).
44. Rabouw HH et al. Inhibition of the integrated stress response by viral proteins that block p-eIF2–eIF2B association. Nat Microbiol 5, 1361–1373 (2020). [PubMed: 32690955]
45. Agarwal P, Gordon S & Martinez FO Foam Cell Macrophages in Tuberculosis. Front Immunol 12, 775326 (2021). [PubMed: 34975863]
46. Bhattacharya B et al. The integrated stress response mediates necrosis in murine Mycobacterium tuberculosis granulomas. J Clin Invest (2020).
47. Vermeulen I et al. Mycolates of Mycobacterium tuberculosis modulate the flow of cholesterol for bacillary proliferation in murine macrophages. J Lipid Res 58, 709–718 (2017). [PubMed: 28193630]
48. Zhu XG et al. CHP1 Regulates Compartmentalized Glycerolipid Synthesis by Activating GPAT4. Mol Cell 74, 45–58.e47 (2019). [PubMed: 30846317]
49. Ouimet M et al. Autophagy regulates cholesterol efflux from macrophage foam cells via lysosomal acid lipase. Cell Metab 13, 655–667 (2011). [PubMed: 21641547]
50. Klionsky DJ et al. Guidelines for the use and interpretation of assays for monitoring autophagy (4th edition)1. Autophagy 17, 1–382 (2021). [PubMed: 33634751]
51. Grootjans J, Kaser A, Kaufman RJ & Blumberg RS The unfolded protein response in immunity and inflammation. Nat Rev Immunol 16, 469–484 (2016). [PubMed: 27346803]
52. Kim MJ et al. Caseation of human tuberculosis granulomas correlates with elevated host lipid metabolism. EMBO Mol Med 2, 258–274 (2010). [PubMed: 20597103]
53. Berry MPR et al. An interferon-inducible neutrophil-driven blood transcriptional signature in human tuberculosis. Nature; 2010. pp. 973–977.
54. Volmer R & Ron D Lipid-dependent regulation of the unfolded protein response. Current Opinion in Cell Biology 33, 67–73 (2015). [PubMed: 25543896]
55. Fu S et al. Aberrant lipid metabolism disrupts calcium homeostasis causing liver endoplasmic reticulum stress in obesity. Nature 473, 528–531 (2011). [PubMed: 21532591]
56. Krzyzosiak A et al. Target-Based Discovery of an Inhibitor of the Regulatory Phosphatase PPP1R15B. Cell 174, 1216–1228 e1219 (2018). [PubMed: 30057111]

57. Rabouw HH et al. Small molecule ISRIB suppresses the integrated stress response within a defined window of activation. Proceedings of the National Academy of Sciences of the United States of America 116, 2097–2102 (2019). [PubMed: 30674674]
58. Han J & Kaufman RJ The role of ER stress in lipid metabolism and lipotoxicity. J Lipid Res 57, 1329–1338 (2016). [PubMed: 27146479]
59. Qin S, Yin J & Huang K Free Fatty Acids Increase Intracellular Lipid Accumulation and Oxidative Stress by Modulating PPARα and SREBP-1c in L-02 Cells. Lipids 51, 797–805 (2016). [PubMed: 27270405]
60. Fineran P et al. Pathogenic mycobacteria achieve cellular persistence by inhibiting the Niemann-Pick Type C disease cellular pathway. Wellcome Open Res 1, 18 (2016). [PubMed: 28008422]
61. Ramakrishnan L Revisiting the role of the granuloma in tuberculosis. Nature reviews Immunology 12, 352 366 (2012).
62. Raines LN et al. PERK is a critical metabolic hub for immunosuppressive function in macrophages. Nature Immunology, 1–15 (2022). [PubMed: 34789862]
63. Cornil V & Ranvier L A manual of pathological histology translated with notes and additions by EO Shakespeare and JHC Simms. Philadephia: Henry C Lea, 394–445 (1880).
64. Im JG, Itoh H, Lee KS & Han MC CT-pathology correlation of pulmonary tuberculosis. Crit Rev Diagn Imaging 36, 227–285 (1995). [PubMed: 7546270]
65. Hunter RL Tuberculosis as a three-act play: A new paradigm for the pathogenesis of pulmonary tuberculosis. Tuberculosis (Edinb) 97, 8–17 (2016). [PubMed: 26980490]
66. Gerner MY, Kastenmuller W, Ifrim I, Kabat J & Germain RN Histo-cytometry: a method for highly multiplex quantitative tissue imaging analysis applied to dendritic cell subset microanatomy in lymph nodes. Immunity 37, 364–376 (2012). [PubMed: 22863836]
67. McQuattie-Pimentel AC et al. The lung microenvironment shapes a dysfunctional response of alveolar macrophages in aging. J Clin Invest 131, e140299 (2021). [PubMed: 33586677]
68. Montague TG, Cruz JM, Gagnon JA, Church GM & Valen E CHOPCHOP: a CRISPR/Cas9 and TALEN web tool for genome editing. Nucleic Acids Res 42, W401–407 (2014). [PubMed: 24861617]
69. Wickham H et al. Welcome to the Tidyverse. Journal of Open Source Software 4, 1686–1686 (2019).
70. Durinck S et al. BioMart and Bioconductor: a powerful link between biological databases and microarray data analysis. Bioinformatics 21, 3439–3440 (2005). [PubMed: 16082012]
71. Robinson MD, McCarthy DJ & Smyth GK edgeR: a Bioconductor package for differential expression analysis of digital gene expression data. Bioinformatics (Oxford, England) 26, 139–140 (2010). [PubMed: 19910308]
72. Ritchie ME et al. limma powers differential expression analyses for RNA-sequencing and microarray studies. Nucleic acids research 43, e47–e47 (2015). [PubMed: 25605792]

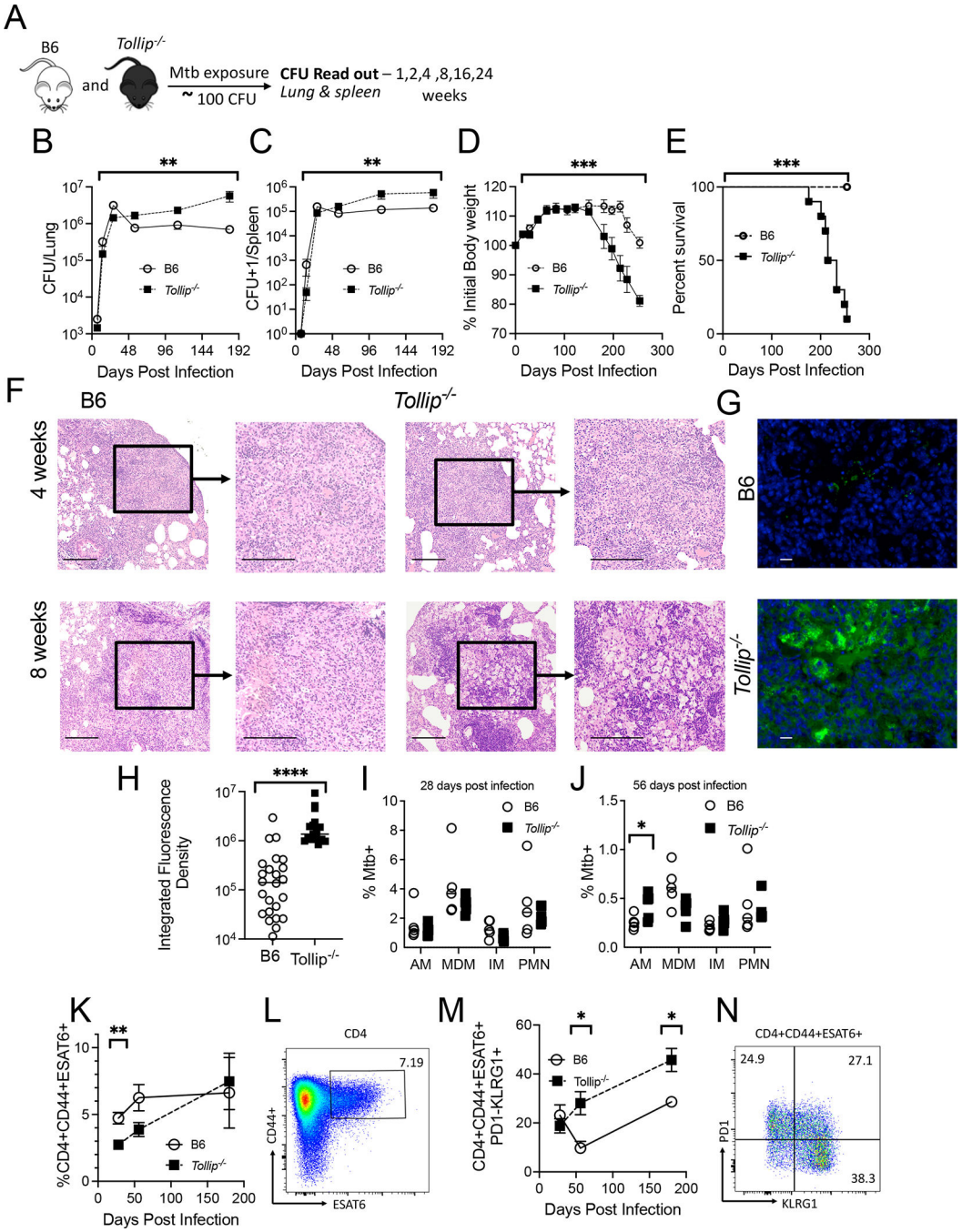

Figure 1. TOLLIP is required for Mtb control in mice

A) Experimental timeline.

B-C) Bacterial burden in B6 (*clear circle*) and *Tollip*$^{-/-}$ (*black square*) mice in **B)** lung (p = 0.0016) and **C)** spleen (p = 0.0092). ** p < 0.01 *** p < 0.001, two-sided mixed effects model. n = 50. Error bars – SEM.

D) Percentage of initial body weight. *Circle* – B6 mice; *square* - *Tollip*$^{-/-}$ mice. N = 20 *** p < 0.001, P = 0.0005, two-way ANOVA accounting for time and genotype. Error bars – SEM.

E) Survival curve analysis of B6 (*clear circle*) and *Tollip*$^{-/-}$ (*black square*) mice after aerosol infection. N = 20. *** $p < 0.001$, two-sided Mantel-Cox test.
F) Hematoxylin and eosin stained lung tissue 28 and 56 days after Mtb infection. Low magnification scale bar - 250μm. High magnification scale bar - 100μm.
G-H) Fluorescence lipid staining in Mtb-infected lungs 56 days after infection. Lipid (*green*) and DAPI (*blue*); scale bar – 10μm.
H) Integrated fluorescence density of lipid staining (area of excess fluorescence above background x fluorescence intensity). N = 20 fields / genotype of four independent experiments. **** $p < 0.0001$, two-sided Mann-Whitney test.
I-J) The percentage of Mtb-infected (mCherry+) alveolar macrophages (AM), monocyte-derived macrophages (MDM), interstitial macrophages (IM), and neutrophils (PMN) **G)** 28 and **H)** 56 days after infection. n = 5/group; * $p < 0.05$, two-sided t-test.
K-L) The proportion of lung-resident **K)** ESAT6(4–17)+CD44+CD4+ T cells after Mtb infection. **L)** Representative image. N = 5 / group 28 ($p=0.002$) and 56 days after infection, N = 4 180 days after infection. * $p<0.05$, two-sided t-test. Error bars – SEM.
M-N) The proportion of **M)** PD1-KLRG1+ESAT6+CD4+CD44+ T cells and **N)** representative image after Mtb infection. N = 9 mice / genotype at days 28 and 56 ($p=0.016$), n = 4 mice/genotype at day 180 ($p=0.007$) after infection, error bars represent SEM. * $p<0.05$, ** $p<0.01$, two-sided t-test.

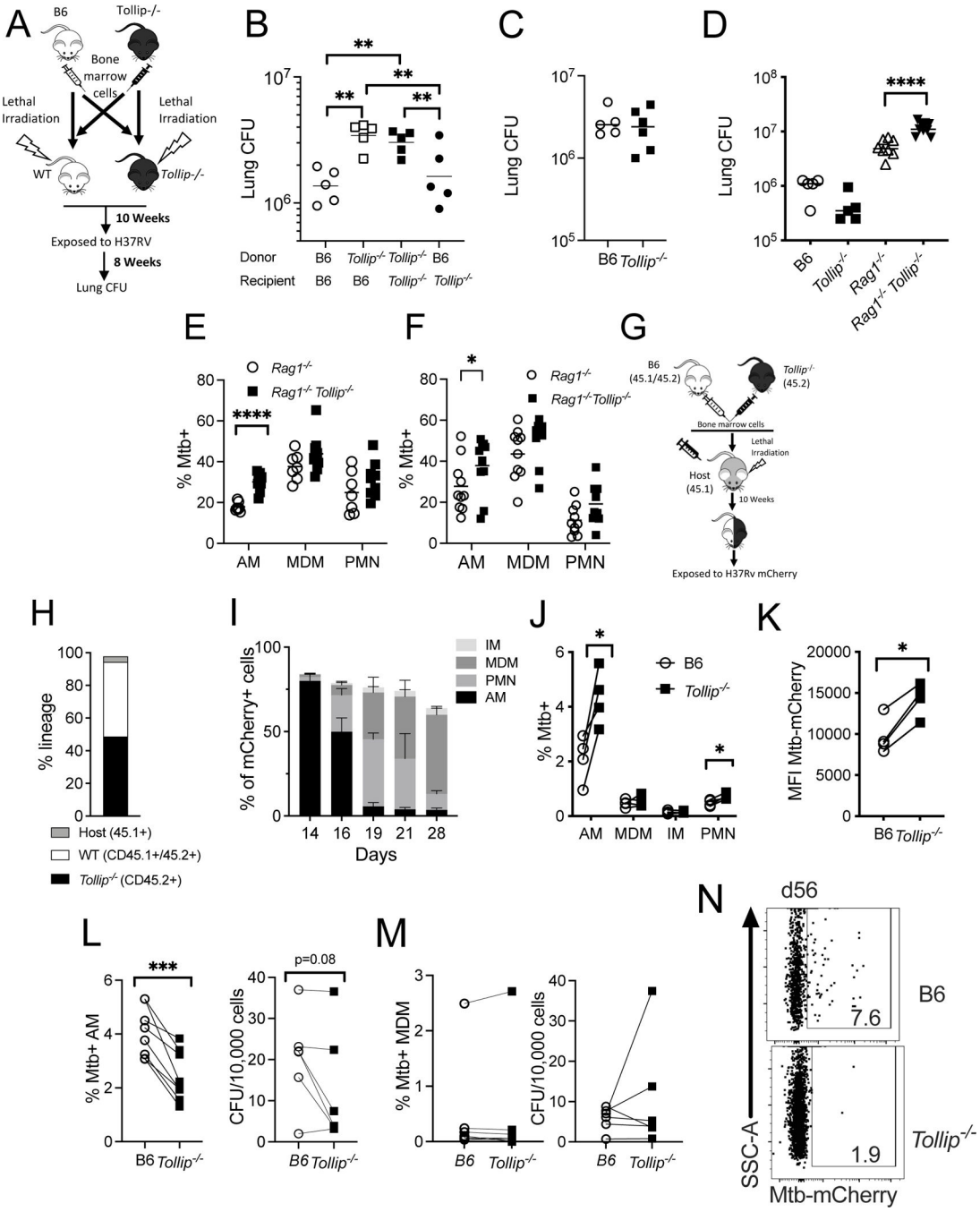

Figure 2. *Tollip*$^{-/-}$ AM exhibit diminished Mtb intracellular carriage in a cell-autonomous manner

A) Experimental outline.

B) Lung bacterial burden in chimeric mice 56 days after Mtb infection (dpi). N = 20. * $p < 0.05$, ** $p < 0.01$. Two-sided ANOVA with Tukey's test. P = 0.0023 for B6B6 vs Tollip−/−B6, p= 0.01 for B6B6 vs Tollip−/−Tollip−/−, p =0.043 for Tollip−/−Tollip−/− vs B6Tollip-/−.

C) Bacterial burden in T cell chimeric mice lungs 56 dpi. N = 11. * p < 0.05, ** p < 0.01, *** p < 0.001, **** p<0.0001, two-sided t-test.
D) Bacterial burden in the lungs of B6 (n = 5), *Tollip*$^{-/-}$ (n = 5), *Rag1*$^{-/-}$ (n = 8), and *Rag1*$^{-/-}$*Tollip*$^{-/-}$ (n = 9) mice 28 dpi. * p < 0.05, ** p < 0.01, *** p < 0.001, **** p<0.0001, two-sided t-test.
E-F) Proportion of Mtb-infected (mCherry+) alveolar macrophages (AM), monocyte-derived macrophages (MDM), and neutrophils (PMN) from *Rag1*$^{-/-}$ (*clear circle*) and *Tollip*$^{-/-}$ *Rag1*$^{-/-}$ (*black square*) mice **E)** 28 (n = 17) and **F)** 44 (n = 22) dpi. P = 0.04 for 2F. * p < 0.05, ** p <0.01, *** p < 0.001, **** p < 0.0001; two-sided t-test.
G) Mixed bone marrow chimera experimental outline.
H) Distribution of CD45 expression in naïve mixed bone marrow chimeric mice. N = 8.
I) Composition of mCherry+ cells among measured lung myeloid cell subpopulations after Mtb infection. N = 5, Bars - mean; error bar - SD.
J-K) The proportion of **J)** Mtb-infected lung-specific myeloid cells (P=0.015 for AM and p=0.023 for PMN) and **K)** MFI of mCherry in Mtb+ AM 28 dpi (p = 0.0076) in mixed bone marrow chimeric mice. Lines connect genotypes from paired samples. * p < 0.05, ** p < 0.01, paired two-sided t-test. N = 5/group.
L-M) The proportion of Mtb-infected and Mtb CFU / 1000 from sorted **L)** AM (p=0.0004 and p=0.08, respectively) or **M)** MDM from mixed bone marrow chimeric mice 56 dpi. Lines connect B6 (*white circle*) and *Tollip*$^{-/-}$ (*black square*) genotypes. *** p < 0.001, paired two-sided t-test. N = 7/group.
N) Representative images from **M**.

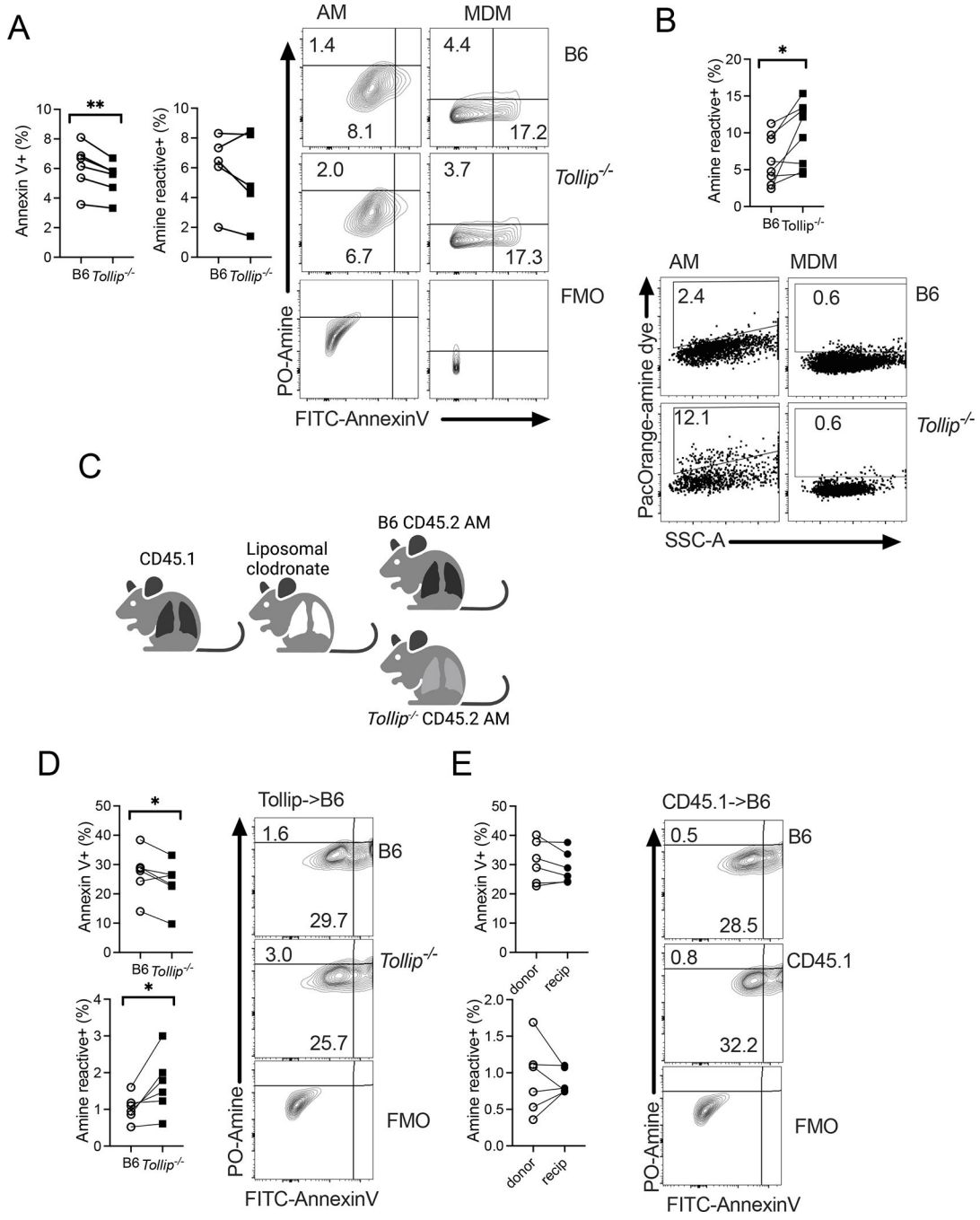

Figure 3. *Tollip*$^{-/-}$ AM undergo increased necrosis in a cell-autonomous manner during prolonged Mtb infection

A) Proportion of apoptotic (Annexin V+) and necrotic (amine reactive dye+) AM from mixed bone marrow chimeric mice 28 days after infection, stratified by genotype. Lines connect B6 (*white circle*) and *Tollip*$^{-/-}$ (*black square*) genotypes from paired samples. P = 0.005. ** p < 0.01, paired two-sided t-test. N = 5. Representative images from B6 and *Tollip*$^{-/-}$ genotype with Annexin V flow minus one (FMO) control are shown,

demonstrating proportions of amine-reactive dye+Annexin V- (necrotic) cells on the top line, and total proportion of Annexin V+ cells (apoptotic) on the bottom line.

B) Proportion of necrotic AM (amine reactive dye+) in mixed bone marrow chimeric mice 56 days after Mtb infection with representative images. Lines connect B6 (*white circle*) and *Tollip*$^{-/-}$ (*black square*) genotypes from paired samples. P=0.021. * $p < 0.05$, paired two-sided t-test. N = 5.

C) Experimental outline of AM adoptive transfer.

D) Proportion of apoptotic (Annexin V+; p = 0.04) and necrotic (amine reactive dye+; p=0.02) *Tollip*$^{-/-}$ (*black square*) donor AM transferred into CD45.1 mice compared with CD45.1+ recipient AM (*white circle*). Lines connect AM from the same animal. * $p < 0.05$, paired two-sided t-test. N = 5. Representative images from B6 and *Tollip*$^{-/-}$ genotype with Annexin V flow minus one (FMO) control are shown. The top number represents the proportion of amine-reactive dye+Annexin V- (necrotic) cells, and the bottom number represents the proportion of Annexin V+ cells (apoptotic).

E) The proportion of apoptotic and necrotic AM in B6 donor (*white circle*) and CD45.1 recipient (*black circle*) AM 56 days after aerosol Mtb infection. Paired two-sided t-test. N = 5/group. Representative images from B6 and *Tollip*$^{-/-}$ genotype with flow minus one (FMO) control are shown. All experiments were performed at least three times for reproducibility.

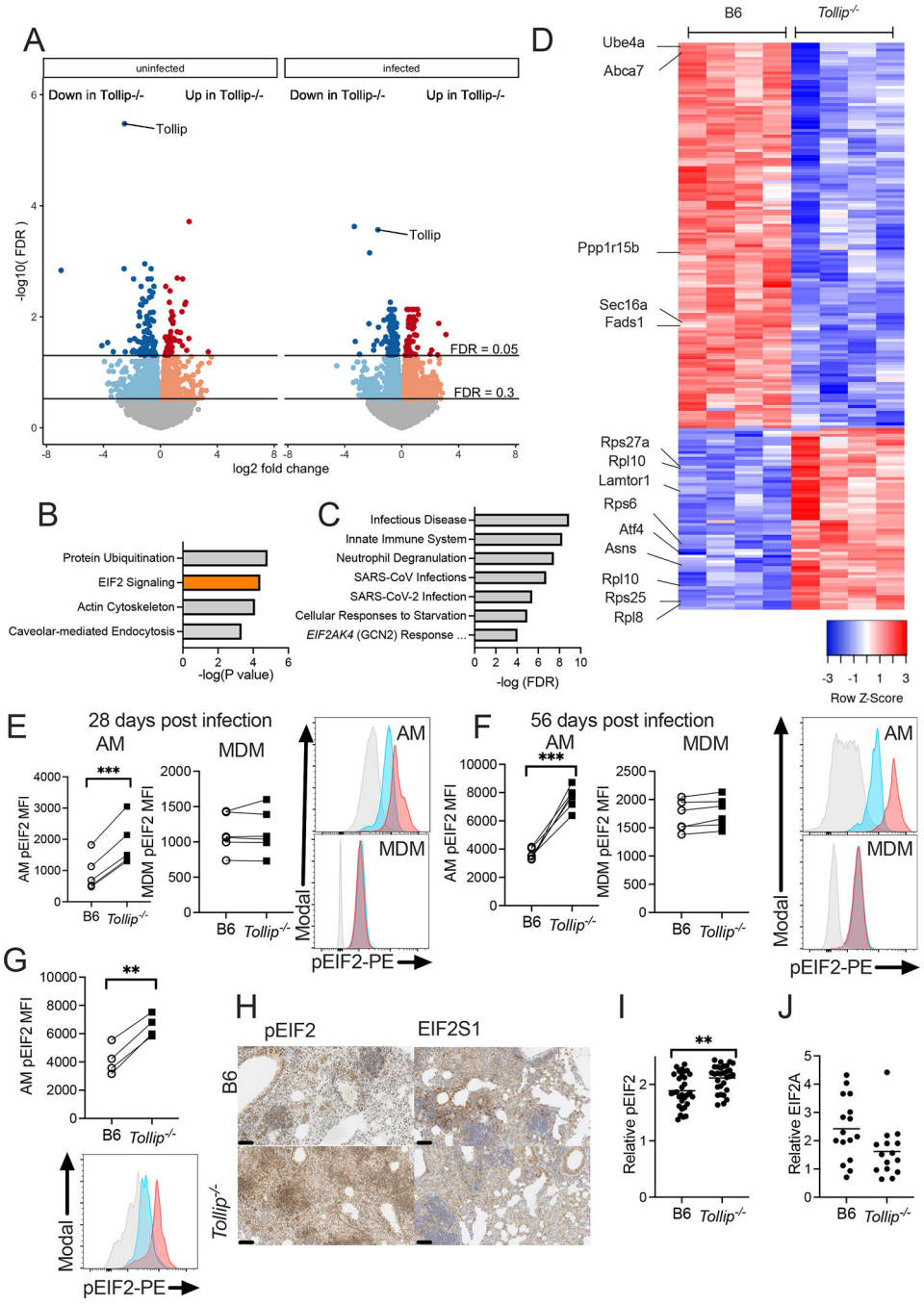

Figure 4. *Tollip*$^{-/-}$ AM autonomously develop increased EIF2 phosphorylation after prolonged Mtb infection

A) Volcano plot of gene expression (log2 fold change) and significance (-log10(FDR)) for genes between *Tollip*$^{-/-}$ (CD45.2) and B6 (CD45.1+CD45.2+) in Mtb-uninfected and Mtb-infected alveolar macrophages (AMs) sorted from mixed bone marrow chimeric mice 28 days after infection (dpi). Horizontal lines indicate differentially expressed genes (DEGs; FDR q < 0.05) and genes of interest (FDR q < 0.3).

B) Ingenuity Causal Network Analysis on DEGs between B6 and *Tollip*$^{-/-}$ Mtb-infected AM (FDR q < 0.05). P value cutoff = 5×10^{-3}, calculated using two-sided Fisher's exact test.
C) Gene set enrichment analysis of DEGs (FDR q<0.05) for Reactome pathways. FDR cutoff $<10^{-4}$ to account for multiple comparisons. Reactome pathway cut off with ellipsis is "Response of *EIF2AK4* (GCN2) to Amino Acid Starvation."
D) Heatmap of gene expression (log2 fold change over average of B6 AM) for DEGs between Mtb-infected AM. Columns are independent experiments of pooled mice, and rows are genes. Called genes are stress response genes of interest.
E-F) pEIF2 MFI in AM and monocyte-derived macrophages (MDM) from mixed bone marrow chimeric mice **D)** 28 days (p=0.003) and **E)** 56 (p=0.002) dpi. B6 – *clear circle*, *Tollip*$^{-/-}$ -- *black square;* lines connect genotypes from paired samples. * p < 0.05, ** p < 0.01, paired two-sided t-test. N = 6/group. Representative histograms B6 – *blue*, *Tollip*$^{-/-}$ -- *red,* IgG control – *gray*.
G) pEIF2 MFI in adoptively transferred *Tollip*$^{-/-}$ AM (*black square*) compared to CD45.1+ recipient AM (CD45.1+, *white circle*). N = 4, p=0.001. ** p < 0.01, paired two-sided t-test.
H) Representative pEIF2 and EIF2A stains of lung tissue 56 dpi.
I-J) Semiquantitative analysis of **H)** pEIF2 (p=0.002) and **I)** EIF2A protein expression. Magnification - 20x; scale bar - 100μm. * p < 0.05, ** p < 0.01, two-sided t-test. N = 5 mice/group.100 high-powered fields were sampled for semiquantitative analysis.

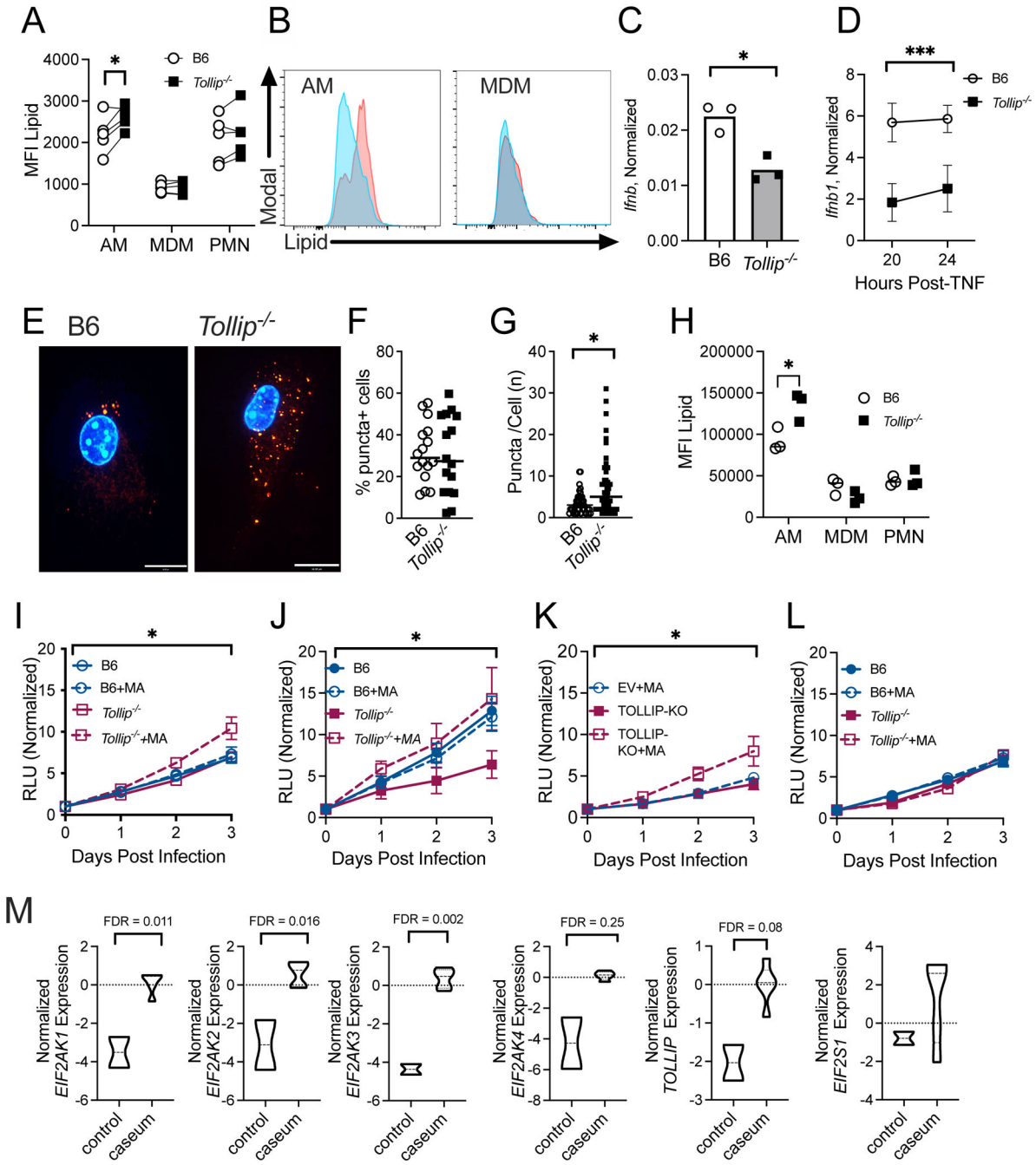

Figure 5. Mycolic acid-treated *Tollip*$^{-/-}$ macrophages accumulate lipids and permit increased Mtb replication

A-B) LipidTox neutral lipid stain MFI in alveolar macrophages (AM; p=0.03), monocyte-derived macrophages (MDM), and neutrophils (PMN) from mixed bone marrow chimeric mice 28 days after Mtb infection (dpi). **B)** Representative histogram of AM and MDM lipid staining (B6 – blue; *Tollip*$^{-/-}$ – red). Lines connect B6 and *Tollip*$^{-/-}$ AM from the same mouse. * $p < 0.05$, paired two-sided t-test; N = 5. Experiment was performed five times.

C) *Ifnb1* mRNA expression, normalized to *Gapdh*, in the lungs of Mtb-infected mice 56 dpi. p=0.009, N = 6 mice over two experiments. B6 (*white circle*) and *Tollip*$^{-/-}$ (*black square*) genotype. * p<0.05, **p<0.01, ***p<0.001, two-sided t-test.
D) Relative *Ifnb1* mRNA expression in B6 (*clear circle*) and *Tollip*$^{-/-}$ (*black square*) AM, normalized to *Gapdh,* after TNF instillation (10 ng/ml). p = 0.01 at 20 hours and p = 0.03 at 24 hours N = 6 replicates in each group over two independent experiments. * p<0.05, **p<0.01, ***p<0.001, two-sided t-test, unadjusted for comparisons. Error bars – SEM.
E-G) Representative lipid staining of PEM incubated with mycolic acid (MA) for 72hrs. LipidTOX Red stain (*red*) and DAPI (*blue*). Magnification 100x; scale bar 16μm. **F)** Percentage of PEM with lipid droplets (LD) and **G)** total number of LD per cell (p=0.002). 100 cells imaged. Bar – mean value.
H) LipidTox neutral lipid stain MFI in alveolar macrophages (AM; p=0.03), MDM, and PMN 5 days after intratracheal MA instillation. *p<0.05, two-sided t-test
I-L) Relative luminescence (RLU) of B6 and *Tollip*$^{-/-}$ **I)** PEM (p=0.03), **J)** AM (p=0.05), **K)** TOLLIP-deficient THP-1 (TOLLIP-KO; p=0.001), and **L)** BMDM after Mtb H37Rv-lux infection, normalized to initial luminescence.; N = 6 over three independent experiments. * p < 0.05; 3-way ANOVA for an effect of MA on *Tollip*$^{-/-}$ macrophages. Error bars – SEM.
M) *EIF2AK1, EIF2AK2, EIF2AK3, EIF2AK4, TOLLIP,* and *EIF2S1* expression in human caseous granuloma tissue compared with healthy-appearing lung tissue from different lobes in the same individuals, normalized to median value. Data are from GSE20050. FDR is indicated above each data point.

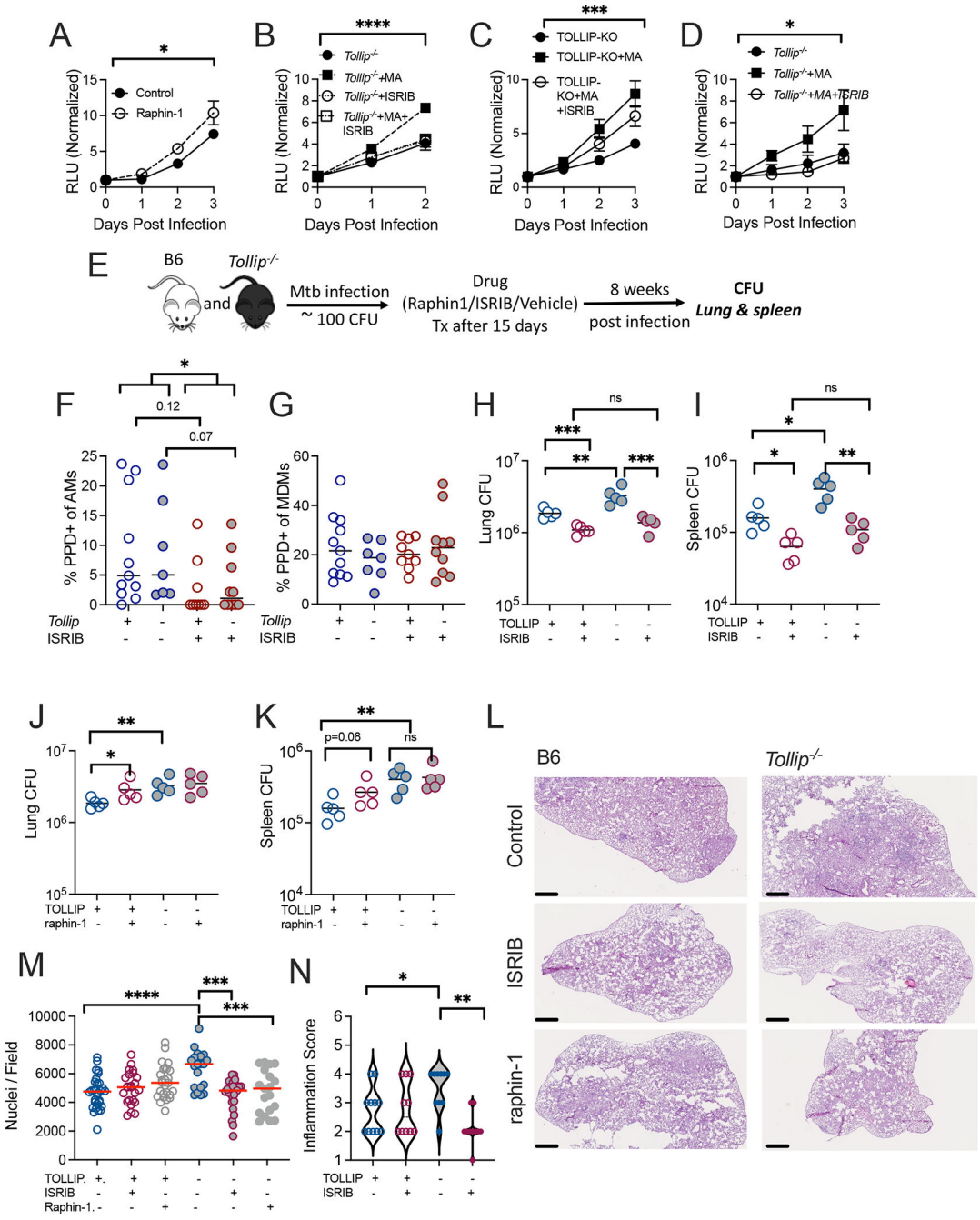

Figure 6. ISRIB treatment restores immune control in *Tollip*$^{-/-}$ mice

A) Relative luminescence (RLU) in B6 peritoneal macrophages (PEM) treated with raphin-1 (*black and white circles*; 10μM) over time. Error bars -- SEM. P = 0.02; * p < 0.05; 2-way ANOVA for an effect of raphin-1 controlling for time. N = 6, experiment was performed three times.

B-D) Normalized RLU was measured 24–72 hours after after Mtb-lux infection in *Tollip*$^{-/-}$ **B)** PEM (p=0.008), **C)** alveolar macrophages (AM; p=0.03), and **D)** THP-1 lacking TOLLIP (TOLLIP-KO; p=0.001). * p < 0.05, ** p < 0.01, *** p < 0.001, **** p< 0.0001, 2-way

ANOVA accounting for time and drug treatment. N = 6, experiment was performed three times. Error bars – SEM.

E) Experimental design. B6 and *Tollip*$^{-/-}$ mice were infected with 50–100 colony forming units (CFU) of Mtb and 15 days after infection, vehicle control, ISRIB (1 mg/kg/day), or raphin-1 (1 mg/kg/day) were instilled intraperitoneally. Eight weeks after infection, mice were euthanized, bacterial CFU was measured, and tissue was collected for pathology analysis. N = 22.

F-G) The percentage of purified protein-derivative-expressing (PPD+) **F)** AM (SiglecF+) and **G)** monocyte-derived macrophages (MDM; CD11b+) in Mtb-infected lung tissue, measured by multiparameter confocal microscopy.

H-I) Mtb CFU in **H)** lungs and **I)** spleen from mice treated with ISRIB.

J-K) Mtb CFU in **J)** lungs and **K)** spleen from mice treated with raphin-1.

L) Representative images of lung tissue from B6 and *Tollip*$^{-/-}$ mice, stained with hematoxylin and eosin. Magnification 5x; scale bar – 500μm.

M) Number of nucleated cells per 20x high-powered field in Mtb-infected mice after ISRIB and raphin-1 treatment. B6 vs. *Tollip*$^{-/-}$ p = 0.0001, *Tollip*$^{-/-}$ vs *Tollip*$^{-/-}$ with ISRIB p <0.0001, *Tollip*$^{-/-}$ vs *Tollip*$^{-/-}$ with raphin-1 p =0.0013. * p < 0.05, ** p < 0.01, *** p < 0.001, **** p< 0.0001, 2-way ANOVA accounting for genotype and drug treatment. N = 11 total.

N) Lung inflammation score, from a blinded veterinary pathologist, after 56 days of Mtb infection. N = 30 mice total. B6 vs. *Tollip*$^{-/-}$ p = 0.02, *Tollip*$^{-/-}$ vs *Tollip*$^{-/-}$ with ISRIB p = 0.001. * p < 0.05, ** p<0.01, 2-sided t-test.